

Diffractionless flow of light in two- and three-dimensional photonic band gap heterostructures: Theory, design rules, and simulations

Alongkarn Chutinan and Sajeev John

Department of Physics, University of Toronto, 60 St. George St., Toronto, Ontario, Canada M5S 1A7

(Received 28 April 2004; published 14 February 2005)

We demonstrate on-chip, single-mode, waveguiding of light in air for a variety of 2D-3D photonic band gap (PBG) heterostructures. These include square spiral, woodpile, slanted pore, and inverse opal three-dimensional (3D) photonic crystals intercalated with a 2D (planar) photonic crystal microchip. Design rules are established to yield maximal single-mode waveguiding bandwidths of up to roughly 180 nanometers centered at a wavelength of 1.5 microns. This can be achieved with 3D PBG materials with gaps as small as 15% of the PBG center frequency. Finite-difference time-domain (FDTD) simulations of light flow in optical microcircuits within such heterostructures reveal tolerance to layer misalignment and other fabrication-related structural disorder. We provide an interpretation of the universal mechanism for diffractionless light propagation in 2D-3D photonic crystal heterostructures. We demonstrate that planar, on-chip, optical microcircuitry similar to that of two-dimensional (2D) photonic crystals is almost universally achievable within the engineered electromagnetic vacuum of 3D PBG materials.

DOI: 10.1103/PhysRevE.71.026605

PACS number(s): 42.70.Qs

I. INTRODUCTION

Photonic band gap (PBG) materials are engineered optical materials in which the dielectric constant varies periodically on the scale of the optical wavelength [1,2]. In these photonic crystal (PC's), the interplay between certain macroscopic and microscopic scattering resonances of light give rise to a photonic band gap—a range of frequencies in which no electromagnetic waves can propagate inside the crystal. Engineered disruptions in periodicity of the dielectric constant (defects) can be created inside photonic crystals. These lead to localized electromagnetic modes that can perform certain prescribed functions. The defects can act, for example, as laser microcavities, waveguides with sharp bends, optical switches, and wavelength multiplexors and demultiplexors [3–12]. Confinement of light by interference-based localization [13] is significantly more robust than more conventional confinement mechanisms based on total internal reflection.

Designs of various components for optical integrated circuits have been presented theoretically in the case of idealized 2D photonic crystals [4,5]. In the case of air waveguides or defects in 2D PC's, there is nothing to prevent light from escaping into the third dimension. Likewise, for dielectric waveguides, confinement of light in the third dimension by total internal reflection is not robust to deviations from periodicity in the waveguiding direction or unintentional forms of random disorder. In either case, light flow in a 2D PC is strongly attenuated by leakage into the third dimension, severely degrading the functionality of the microchip for integrated optics. For practical realization, three-dimensional photonic crystals with a complete PBG offer profound advantages in confining light through the mechanism of localization inside submicron scale circuits. Moreover, it is possible to engineer the electromagnetic vacuum within a 3D PBG for frequency selective control of spontaneous emission and the possibility of on-chip integration of novel active devices [14]. While the potential for 3D PBG materials as base

media for integrated all-optical microcircuits has been alluded to [3,10,11], a comprehensive and general set of design rules, applicable to any type of 3D PBG structure, has been lacking up to now. Although designs for single-mode, air waveguide channels inside specific structures [6,7,11] have been presented, such design strategies are not readily applicable to other types of 3D PBG structures. Recently, we have proposed the concept of 2D-3D heterostructures as a versatile and universal approach to integrated optics in PBG materials. The 2D-3D heterostructures are a combination of 2D and 3D structures wherein a thin 2D PC membrane containing optical microcircuits is sandwiched in between two 3D PBG materials above and below that act as cladding layers to completely confine the light [15]. In this paper we present extensive analyses and illustrative results on a variety of 2D-3D heterostructures supporting diffractionless flow of light within optical microcircuits. These include microchips based on square spirals [16–18], woodpile [6,10,19,20], slanted pore [21], Yablonovite [22], and inverse opal PBG structures [23–25]. We also provide a detailed explanation on the mechanism of light confinement and confinement within the 2D-3D heterostructures.

We begin in Sec. II by discussing general characteristics of our heterostructure design and their relationship to the goal of achieving high-bandwidth, lossless, optical microcircuitry. In Sec. III, we describe computational methods used in this paper. These include the plane-wave (PW) expansion method and the finite-difference time-domain method (FDTD). In Sec. IV, the optical microchip based on the square spiral heterostructure [16–18] is presented in detail. It is shown how the properties of heterostructures depend on various structural parameters such as relative position of 2D PC slab and thickness of slab. In particular, it is shown that a class of heterostructures based on the so-called direct [001]-diamond:1 square spiral 3D PBG (see Sec. IV) exhibit exceptionally strong tolerances against the structural disorders. In Secs. V–VII, optical microchips based on the

woodpile [6,10,19,20], slanted pore [21], Yablonovite [22], and inverse opal [23–25] PBG heterostructures are described. In Sec. VIII, the decrease of the waveguiding bandwidth and optical backscattering losses due to surface roughness and other unintentional structural disorder are investigated. In Sec. IX, we illustrate the unique functionality of our designs by comparing and contrasting them with heterostructures using a simpler 2D and 1D photonic crystal design. In particular, we demonstrate that if the 2D optical microchip layer is sandwiched between a pair of 1D omnidirectional reflectors [26,27], light from the microchip can easily escape into the third dimension. Finally, we present a detailed analysis and interpretation of the mechanism for high bandwidth light flow and confinement within our 2D-3D PBG heterostructures in Sec. X. Concluding remarks are presented in Sec. XI.

II. DESIGN CONSIDERATIONS

Without specific design objectives, there are innumerable ways to combine 2D and 3D photonic crystals. However, the requirement of optimal bandwidth, single-mode flow of light through waveguide channels on a 2D microchip layer leads to a nearly unique, but universally applicable, set of design rules. In this section, we discuss the physical properties of the 2D-3D heterostructures required to achieve these design objectives.

One goal of the 2D-3D heterostructure is to eliminate the leaky modes from the free-standing 2D PC slab by using the omnidirectional band gap of the 3D PBG cladding layers. This suggests that the entire 2D-3D heterostructure should possess a 3D PBG. The size of the 3D PBG may be smaller within or near the 2D PC microchip layer than it is far away from the 2D PC layer. The 2D PC slab may be regarded as a planar defect within the 3D PBG material that induces electromagnetic modes within the 3D PBG. The aim of our design is to confine any spurious defect modes into a small spectral region within the PBG of the cladding. The remaining spectral range (containing no planar defect modes) within the 3D PBG is referred to as the “on-chip 3D PBG.” Additional point and line defects within the 2D microchip layer may induce additional defect modes within the on-chip 3D PBG, leading to the desired optical microcircuitry. Note that the on-chip PBG cannot be larger than the bulk 3D PBGs of the cladding layers. Also the 2D PC slab, by itself, does not possess an omnidirectional band gap. Our design objectives are that the 3D cladding layers will (i) prevent light from leaking out of the 2D PC slab layer and (ii) enable diffractionless optical circuits using defect cavities, waveguides, waveguide bends inside the 2D PC layer in a manner analogous to the infinitely high 2D PC [28]. The difference is that these defect modes will lie inside the on-chip 3D PBG, rather than the 2D band gap.

In designing 2D-3D heterostructures that fulfill points (i) and (ii) above, with maximum possible bandwidth, there are two types of 2D PC layers that can be considered. One is the structure with air rods in dielectric background and the other is the structure with dielectric rods in air background. Both are viable, but we concentrate here on the latter. For the waveguide structure, we choose to use air waveguides con-

sisting of a single row of missing dielectric rods. Such air waveguides are readily engineered to be single mode while dielectric waveguides with a single row of missing holes tend to be multimode. Single-mode waveguide channels are more robust (exhibit lower scattering losses) to imperfections in manufacturing than their multimode counterparts. In the context of a waveguide channel in a complete, on-chip 3D PBG, small amounts of disorder (such as surface roughness) can nevertheless lead to weak backscattering along the axis of the waveguide.

We begin by cutting the 3D PBG material into two fractions and inserting a thin layer of the 2D PC in between (as opposed to replacing part of the 3D PBG material by the 2D PC layer). For the 2D-3D heterostructure to be periodic in the plane defined by the microchip layer, it is necessary to match the lattice type and lattice constant of the 2D PC slab with those seen at the cross section of the 3D PBG cladding. Consider for example, the recently introduced [16–18] square spiral 3D PBG material. While seemingly complex in architecture, this 3D PBG cladding can be rapidly synthesized [18] in a single step of deposition. If we choose to cut the square spiral structure at the plane (001), the in-plane lattice type is a square lattice and we denote the lattice constant as a . Therefore, the 2D PC layer must also be a square lattice with the lattice constant a . Another widely studied 3D PBG architecture is the so-called “inverse opal” structure [23–25], consisting of a close-packed fcc lattice of air spheres in a high refractive index background. If we cut the inverse opal structure at the plane (111), the 2D PC layer must be a triangular lattice with lattice constant $a' = a/\sqrt{2}$, where a is the lattice constant of the fcc lattice. There is no theoretical limitation on the choice of plane to cut the 3D PBG. For instance we could consider cutting the inverse opal structure at the (001) plane. However, the specific fabrication process may be simplified by one choice of cutting plane as opposed to another.

Given the general design objectives for useful 2D-3D heterostructures, illustrated above, some specific design parameters must now be chosen. They are listed as follows.

- (1) Position to embed the 2D PC layer.
- (2) Thickness of the 2D PC layer.
- (3) Radius of dielectric rods in 2D PC layer.
- (4) Position to place the rods in the plane of 2D PC layer.

While the choices (1)–(3) may represent degrees of freedom in the heterostructure design, the fourth parameter is rather limited by the connectivity and mechanical stability of the structures. That is, the dielectric rods must be placed on the dielectric materials available at the cross sections of the 3D PBG, not on a void. For optimal mechanical stability, we assume that the dielectric rods are always placed at the center of the dielectric parts visible at the cross sections.

For concreteness, we consider the heterostructure made from the dielectric material whose dielectric constant is equal to 11.9. This describes silicon at wavelength larger than $1.5 \mu\text{m}$ [29]. This dielectric constant will be used for all of the structures considered in this paper.

III. COMPUTATIONAL METHODS

We use two different numerical methods to investigate the properties of photonic crystal heterostructures. The plane-

wave expansion method [30] is employed to obtain the band structures of the 3D PBG cladding layers. A supercell technique is employed to calculate the band structures of the heterostructures. A supercell labeled by (n_x, n_y, n_z) consists of n_x unit cells in the x direction, n_y unit cells in the y direction (where the xy plane defines the plane of the 2D microchip layer), and n_z unit cells in the z direction (normal to the microchip). In our calculation, the unit cell is either that of a simple tetragonal lattice containing one (square spiral [16–18], slanted pore [21]) or two (woodpile [6,10,19,20]) Wigner-Seitz cells or that of a simple orthorhombic lattice containing 6 Wigner-Seitz cells (Yablonovite [22], inverse opal [23–25]). A supercell with the size of $1 \times 1 \times 6$ unit cells (square spiral, woodpile, slanted pore) or $1 \times 1 \times 3$ (Yablonovite, inverse opal) is used to calculate the on-chip band structure of the heterostructure without any on-chip defects. In this case, approximately 1800 plane waves are used to expand the on-chip electromagnetic field. The dispersion relation of the on-chip waveguide mode (with waveguide axis along the x direction) is calculated using a supercell with the size of $1 \times 6 \times 6$ unit cells (square spiral, woodpile, slanted pore) or $1 \times 4 \times 3$ unit cells (Yablonovite, inverse opal). We use up to 9500 plane waves in this case. We note here that by using single-precision numbers and symmetric properties of the Hermitian matrix, the resulting size of matrix occupies less than 2GB of memory and one eigenvalue problem could be solved within more or less than 12 hours using a high-end personal computer. The Fourier coefficients of the dielectric constant of photonic crystals are calculated by using fast Fourier transform (FFT) with the resolution of 80 mesh points per lattice constant (a). We note that it is adequate to calculate the band structure for only the in-plane directions since the other directions are forbidden to wave propagation by the 3D PBG cladding layers.

We use the finite-difference time-domain (FDTD) method [31] to calculate the propagation of light inside the heterostructures. A large FDTD computational domain with secondary order Mur's absorbing boundary conditions (ABC) is used [32]. A pulse with a Gaussian profile in time is sent along the waveguide and the transmitted and reflected pulses are measured. The explicit mathematical expression of the Gaussian pulse used is $\exp\{-[(kt\Delta t - 3t_0)/(t_0)]^2\}$, where kt is the current time step number, Δt is the temporal resolution of FDTD (the length of time interval between two consecutive time steps) and t_0 is equal to $\sqrt{\ln 2}/(\pi f_0)$. This yields a pulse with full width at half maximum (FWHM) $= 2f_0$ in the frequency spectrum. The measured pulses are then Fourier transformed to obtain transmission and reflection spectra of the waveguide bends, waveguides with defects, and waveguides with random disorders. The spatial resolution of our FDTD is 10 mesh points per a , where a is the lattice constant (or $\Delta x = \Delta y = \Delta z = 0.1a$). The temporal resolution is chosen to satisfy the condition for numerical stability of the simulation as follows. $\Delta t = 0.05a/c$, where c is the light speed in vacuum.

IV. SQUARE SPIRAL STRUCTURES

In this section, we describe in detail the 2D-3D heterostructure using various square spiral 3D PBG cladding layers

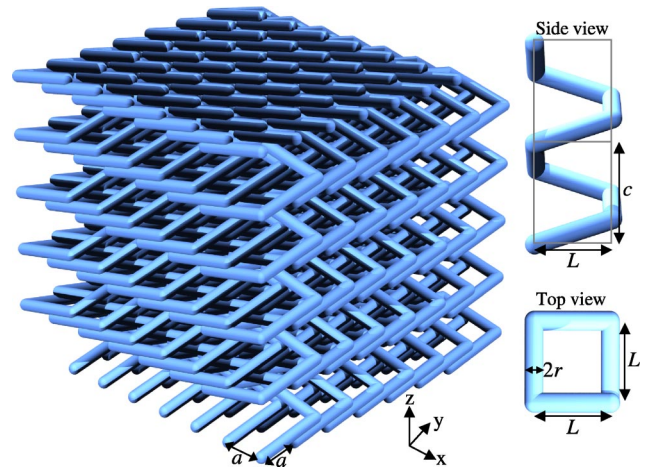


FIG. 1. Schematic of the square spiral structure. The building block of the crystal is made from a coil of pitch c with a single loop whose transverse cross section is a square with edges of length L . The pitch is the same as the lattice constant in the z direction, and the coil is wrapped around the z axis. Each of the segments of the coil is coated with a cylinder of radius r .

and the square lattice 2D PC slab. There are four important spiral PBG architectures [16,17] which we denote as (a) [001]-diamond:5, (b) inverse [001]-diamond:5, (c) [001]-diamond:1, and (d) inverse [001]-diamond:1. The [001]-diamond:1 structure is obtained by approximately connecting the first nearest neighbor lattice points of the diamond structure to form a square spiral along the [001] axis. Each period of the spiral consists of four lattice points. Likewise, the [001]-diamond:5 structure is obtained by connecting the fifth nearest neighbor lattice points. Shown in Fig. 1 is a schematic of the square spiral structure, which consists of square spiral posts in a tetragonal lattice. The structure has a large and robust 3D PBG and is amenable to large-scale microfabrication using glancing angle deposition (GLAD) techniques [18,33]. As shown in Fig. 1, the tetragonal crystal has lattice constants c along the z axis and a along the x and y axes. The building block of the crystal is made from a coil of pitch c (Fig. 1, side view inset) with a single loop whose transverse cross section is a square with sides of length L (Fig. 1, top view inset). The pitch is the same as the lattice constant in the z direction, and the coil is wrapped around the z axis. Each segment of the coil is coated with a cylinder of radius r (Fig. 1, top view inset) whose dielectric constant is ϵ_s . The spirals are embedded in a material whose dielectric constant is ϵ_b . The dielectric constants (ϵ_s, ϵ_b) are (11.9, 1) or (1, 11.9) for the direct or inverse structure, respectively. We discuss here the heterostructure architecture for each of the four types of square spiral 3D PBGs.

A. Direct [001]-diamond:5

Since the on-chip band gap cannot be larger than the band gap of the bulk 3D PBG, we consider the architecture with the largest band gap. We use the optimized direct [001]-diamond:5 with the structural parameters $[L, c, r] = [1.65, 1.30, 0.13]a$. The structure possesses a volume frac-

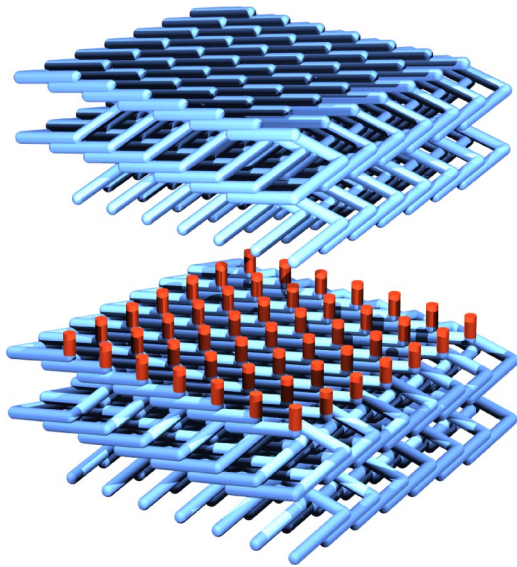


FIG. 2. Schematic of the square spiral structure based heterostructure. The 2D PC layer consisting of a square lattice of circular dielectric rods is placed on top of the lower square spiral 3D PBG cladding layer. The upper 3D PBG cladding layer is separated to help visualize the 2D PC layer.

tion of dielectric materials of $\sim 26\%$ and a 3D PBG in a normalized frequency range $a/\lambda = 0.355 - 0.415$. The size of 3D PBG for this direct structure is $\sim 16\%$ when measured as a percentage of the center frequency. We show in Fig. 2 a schematic of the direct square spiral structure based heterostructure to help visualize the architecture. The detailed discussion on the experimental fabrication of the square spiral structure can be found elsewhere [18].

First, the position to embed the 2D PC layer is investigated. We assume the thickness of the 2D PC slab t to be $c/2 = 0.65a$ and the radius of rod in the 2D PC layer r_{2D} to be the same as r , which is $0.13a$. Since the square spiral has four turns in one period along the vertical direction, it is sufficient to consider the embedding position from $z=0$ (at the elbow) to $z=1/8c$ (at the middle of the spiral arm). As discussed in Sec. II, the dielectric rods of the 2D PC layer are placed on the dielectric parts of the structure and are centered at the centers of corresponding spiral arms. We calculate the band structure for various embedding positions and we summarize the essential conclusion in Fig. 3. Here, the size of the on-chip band gap is plotted as a function of the embedding position. It is seen that the on-chip band gap is largest when the embedding position $z=0$, i.e., when the 2D PC layer are inserted right at the elbow of the spirals. The size of the on-chip band gap decreases monotonically as the embedding position is moved away from the elbow and becomes zero for $z > 0.0385c$. Shown in Figs. 4(a) and 4(b) are the band structures for $z=0$ and $z=1/8c$, respectively. The dark shaded region corresponds to frequency bands of propagating electromagnetic modes while the frequency range $a/\lambda = 0.355 - 0.415$ is the full PBG for the square spiral cladding regions. Two or three planar defect bands inside this frequency range are created by the insertion of the 2D PC layer. We can see that for different embedding positions, the in-

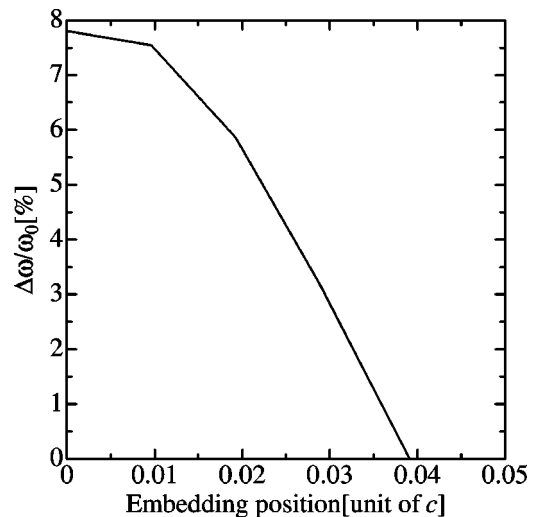


FIG. 3. Size of on-chip band gap as a function of the embedding position for the direct [001]-diamond:5 based heterostructure. The thickness of 2D PC layer is $0.65a$ and the radius of rods in the 2D PC layer is $0.13a$. The size of on-chip band gap is measured as a percentage of the center frequency.

serted 2D PC layer creates completely different defect states. For improper embedding ($z=1/8c$), the planar defect bands span the entire band gap and close it. For ideal embedding ($z=0$), a substantial part of the band gap remains open throughout the heterostructure.

Second, we investigate the effect of varying the thickness of the 2D PC layer. Here, we choose the embedding position $z=0$ and assume the thickness, t , of the 2D PC slab varies over the range $0 < t < 1.0a$ and the radius of rod, r_{2D} , in the 2D PC layer is $0.13a$. Figure 5 shows the change of the on-chip band gap as a function of the 2D PC layer thickness. It is seen that the size of the band gap decreases with the increasing 2D PC layer thickness. This is not unexpected since the thicker 2D PC layer can support more defect modes, thus devouring larger parts of the on-chip band gap. To determine the optimal thickness, we must consider the spectral bandwidth of waveguide channels “written” into the microchip layer (see below).

Third, we examine the radius of rod in the 2D PC layer. Again we fix the embedding position at $z=0$ and choose the thickness to be $0.65a$. The radius of rod is assumed to vary from $0.11a$ to $0.20a$. Figure 6 shows a plot of the size of on-chip band gap (as a percentage of the center frequency) versus the radius of rod. While there exists the maximal on-chip band gap at $r=0.15a$, the reduction of on-chip band gap from the maximal one remains less than 4% throughout the range $0.14a \leq r \leq 0.17a$.

We now consider the creation of a single waveguide mode by removing a row of dielectric rods in the 2D PC layer. We start by assuming $z=0$, $t=0.65a$, and $r_{2D}=0.15a$. Figure 7(a) shows the dispersion relation of the waveguide mode. Again, the dark shaded region corresponds to frequency bands of propagating electromagnetic modes inside the bulk 3D PBG materials. The light shaded region shows the spurious planar defect modes inside the 2D PC layer. Remarkably, the band diagram shows a single waveguide mode that spans the en-

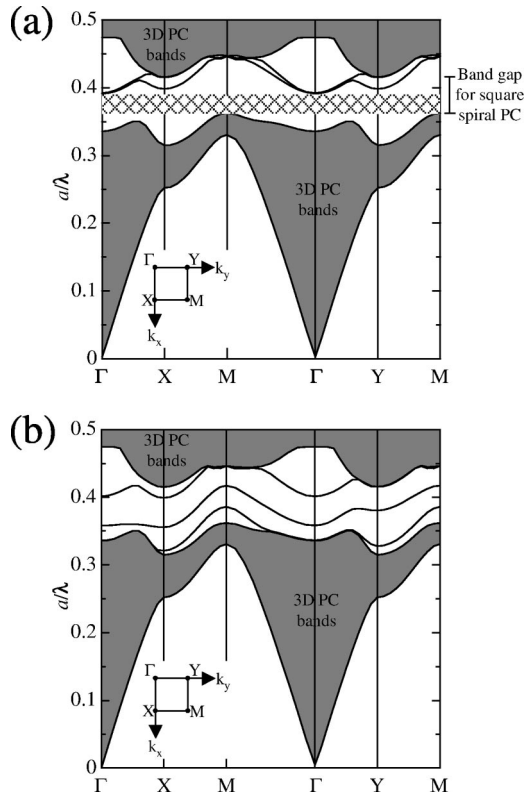


FIG. 4. Band diagrams for the direct [001]-diamond:5 based heterostructures with the embedding position (a) $z=0$ and (b) $z=1/8c$. The thickness of the 2D PC layer is $0.65a$ and the radius of rods in the 2D PC layer is $0.13a$. The dark shaded regions correspond to the frequencies of propagating electromagnetic modes in the bulk 3D PBG material. The hatched region in (a) shows the on-chip band gap obtained after insertion of the 2D PC layer at the position $z=0$.

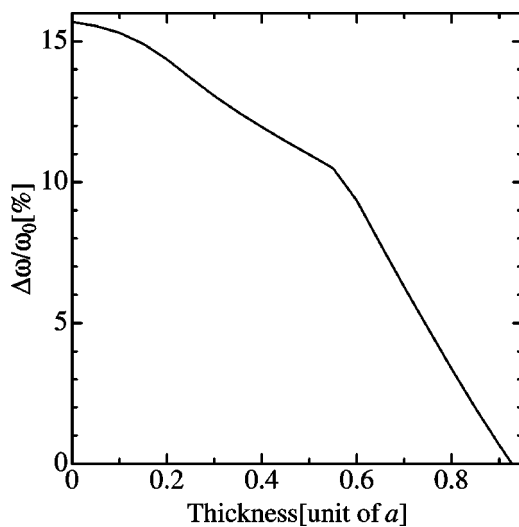


FIG. 5. Size of on-chip band gap as a function of the thickness of 2D PC layer for the direct [001]-diamond:5 based heterostructure. The embedding position is $z=0$ and the radius of rods in the 2D PC layer is $0.13a$.

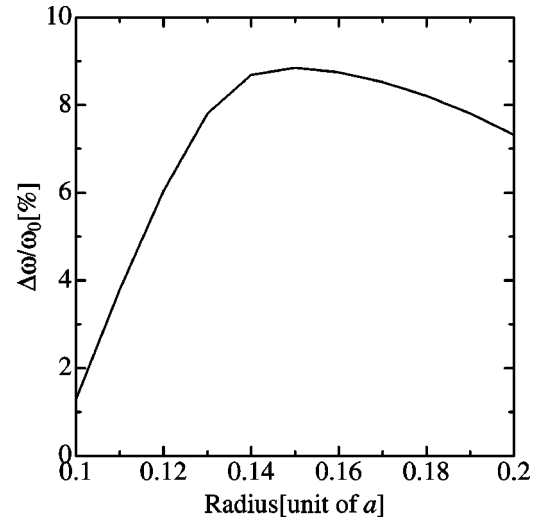


FIG. 6. Size of on-chip band gap as a function of radius of rod in the 2D PC layer for the direct [001]-diamond:5 based heterostructure. The embedding position is $z=0$ and the thickness of 2D PC layer is $0.65a$.

ture on-chip band gap. For the purpose of optimizing the waveguide bandwidth, we re-investigate the thickness of the 2D PC layer. We calculate the band structure for the thickness varying from 0.3 to $0.8a$. Figures 7(b) and 7(c) show the band diagrams for the case $t=0.3a$ and $t=0.8a$, respectively. Clearly, there is a tradeoff between the size of the on-chip PBG and the single-mode air waveguide bandwidth. For a very thin slab, the on-chip band gap is large but the air waveguide mode is flat and spans only a short range of frequencies. For a very thick slab, the on-chip band gap is very small. We plot the waveguiding bandwidth as a function of the thickness t in Fig. 8. The waveguiding bandwidth reaches its maximum of 154.6 nm at $t=0.5a$, and remains well above 151 nm for $0.45a \leq t \leq 0.6a$. This characteristic offers significant tolerance to potential thickness disorder in the manufacturing process. By choosing the thickness within the above range, the air waveguide mode spans more than 150 nm of the on-chip band gap and exhibits a band center group velocity of approximately $0.23c_0$, where c_0 is the velocity of light in vacuum.

Finally, we investigate the effect of varying rod radius on the bandwidth of the waveguide mode. We find that the waveguiding bandwidth remains above 149 nm for $0.13a \leq r \leq 0.19a$ when $t=0.5a$, as shown in Fig. 9. In fact, within the 2D parameter space of $0.13a \leq r \leq 0.19a$ and $0.45a \leq t \leq 0.6a$, the waveguiding bandwidth is larger than 146 nm and the maximum of 154.6 nm is reached when $t=0.5a$ and $r=0.15a$.

B. Inverse [001]-diamond:5

We consider the inverse [001]-diamond:5 structure with the optimal structural parameters $[L, c, r]=[1.5, 1.7, 0.33]a$, corresponding to a dielectric volume fraction of $\sim 21\%$. This structure exhibits a 3D PBG of $\sim 23\%$. We begin by investigating the embedding position. Since the structure is an

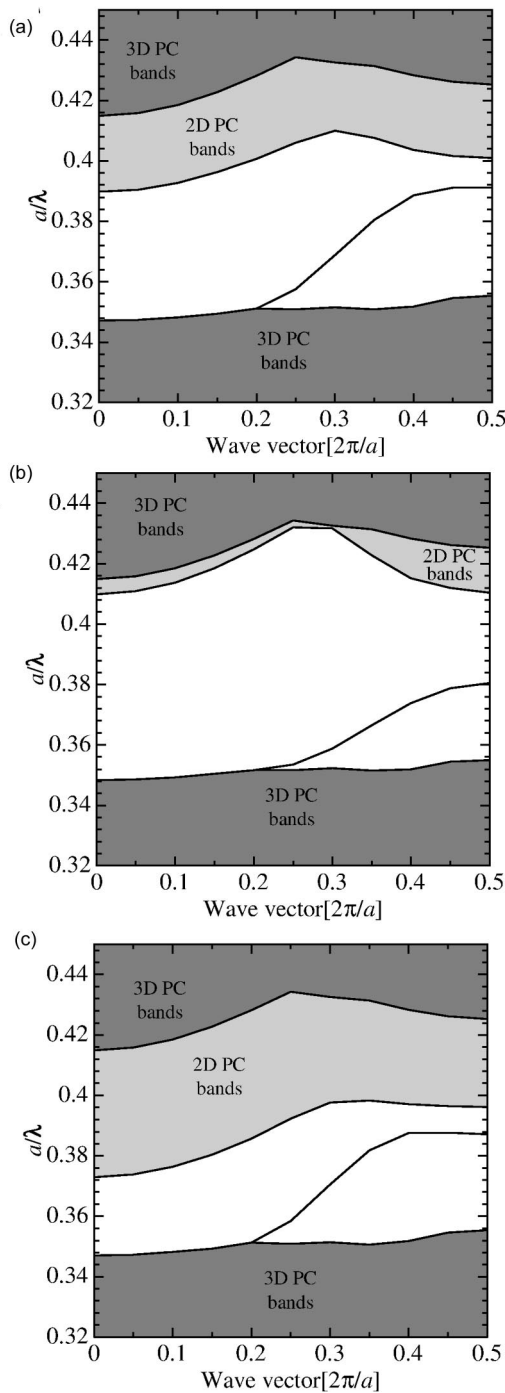


FIG. 7. Dispersion relation for an air waveguide channel within the 2D PC layer obtained by removing one row of dielectric rods in the 2D PC layer of the direct [001]-diamond:5 based heterostructure. The thickness of the 2D PC layer is (a) $t=0.65a$, (b) $t=0.3a$, and (c) $t=0.8a$. The lightly shaded regions indicate the frequencies of propagating modes in the 2D PC layer.

inverse of the square spiral structure, the radius $r=0.33a$ of air spiral will yield an area of approximately $(1-2r)a \times (1-2r)a = 0.34a \times 0.34a$ of dielectric material in one unit cell. Therefore, we assume the radius of rod in the 2D PC layer $r_{2D}=0.17a$, to fit the dielectric area. The 2D PC layer thickness t is set to $0.5a$. We calculate the band structure for

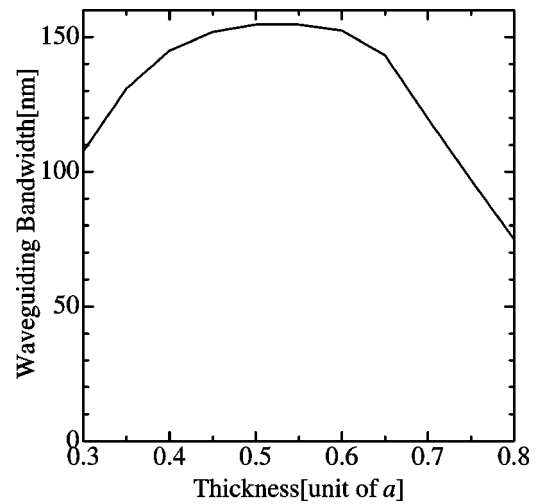


FIG. 8. Waveguiding bandwidth as a function of the thickness t of the 2D PC layer for the direct [001]-diamond:5 based heterostructure. The radius of rod in the 2D PC layer is $0.15a$.

varying embedding position and find that again, the on-chip band gap is the largest when the embedding position is $z=0$, or when the spirals are cut right at the elbows. Similar to the case of direct structures, the size of the on-chip band gap decreases monotonically as the embedding position is moved away from the elbow. The on-chip band gap vanishes for $z > 0.044c$ in this case.

As seen in the previous case, the optimal structural parameters must be determined in the context of single-mode waveguiding bandwidth, rather than simply the size of on-chip band gap. Therefore, we move directly to the examination of the waveguide mode. First, we consider the waveguide created by removing a row of dielectric rods in the 2D PC layer when $z=0$, $t=0.5a$, and $r_{2D}=0.17a$. Figure 10 shows the dispersion relation of the waveguide mode. Again, the band diagram shows a single waveguide mode that spans the entire on-chip band gap.

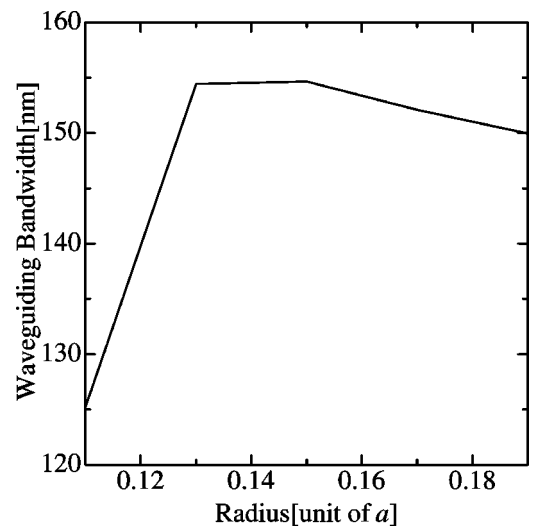


FIG. 9. Waveguiding bandwidth as a function of the radius of rod r in the 2D PC layer for the direct [001]-diamond:5 based heterostructure. The thickness of the 2D PC layer is $0.5a$.

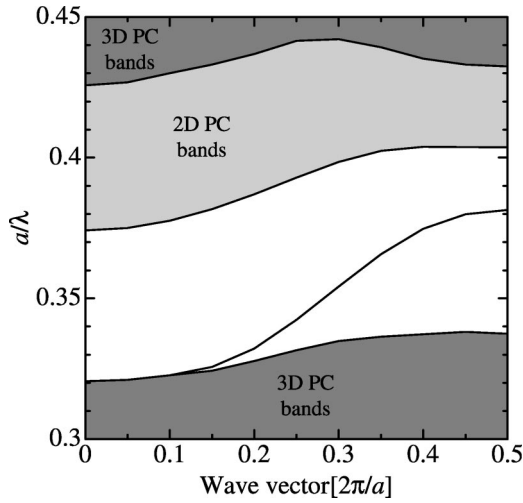


FIG. 10. Dispersion relation for an air waveguide channel obtained by removing one row of dielectric rods in the 2D PC layer of the inverse [001]-diamond:5 square spiral based heterostructure. The thickness of 2D PC layer is $0.5a$ and the radius of rod in the 2D PC layer is $0.17a$.

We scan the structural parameters r from $0.13a$ to $0.21a$ and t from $0.3a$ to $0.8a$ and calculate the waveguiding bandwidth for each case. The results are summarized in Fig. 11. The largest waveguiding bandwidth of ~ 183 nm is obtained when $t=0.45a$, $r=0.17a$. It is seen in Fig. 11 that the waveguiding bandwidth depends strongly on the thickness t but weakly on the radius r .

Next, we use the 3D FDTD to calculate the field pattern of the waveguide mode in the heterostructure. Shown in Figs. 12(a) and 12(b) are the field patterns in the horizontal and the vertical plane, respectively, for the waveguide mode with the wave vector $k=0.25[2\pi/a]$. The field patterns are shown for the case that the thickness of the 2D PC layer is $0.5a$. The field pattern for the infinitely high 2D photonic crystal with the same parameters is also shown in Fig. 12(c), for comparison.

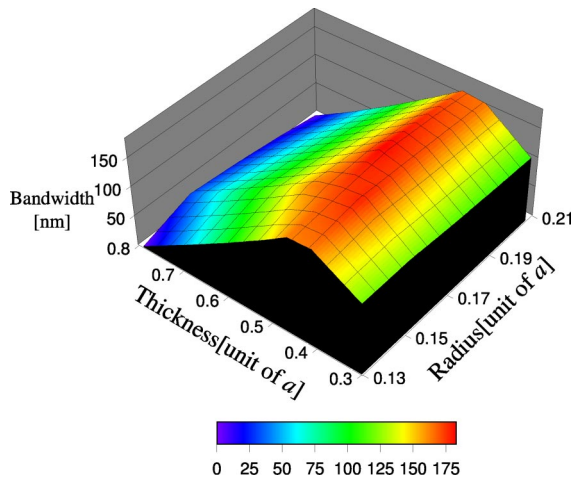


FIG. 11. Waveguiding bandwidth as a function of the thickness of 2D PC layer and the radius of rod in the 2D PC layer for the inverse [001]-diamond:5 square spiral based heterostructure.

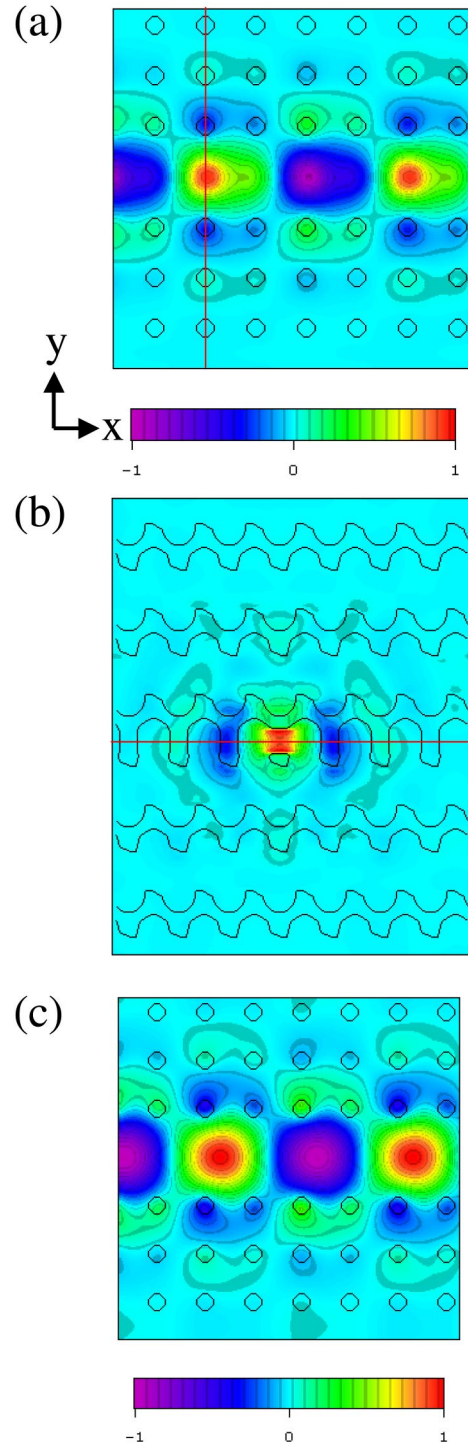


FIG. 12. (a), (b) Distribution of the z -component of electric field for the waveguide mode in the inverse [001]-diamond:5 square spiral based heterostructure at certain cross sections. The thickness of 2D PC layer is $0.5a$ and the radius of rod in the 2D PC layer is $0.17a$. The wave vector is $0.25[2\pi/a]$. (a) x - y plane, at the center of the waveguide [shown by the red line in (b)]. (b) y - z plane, at the center of the dielectric rod [shown by the red (black) line in (a)]. (c) The field pattern for the infinitely high 2D PC with the same parameters, shown for comparison.

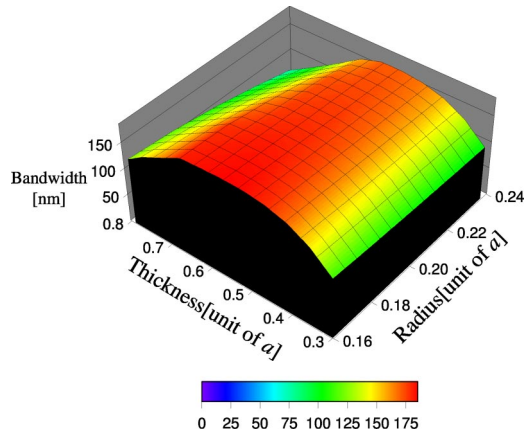


FIG. 13. Waveguiding bandwidth as a function of the thickness of 2D PC layer and the radius of rod in the 2D PC layer for the [001]-diamond:1 square spiral based heterostructure.

C. Direct [001]-diamond:1

From the standpoint of high bandwidth single-mode waveguiding in air, one of the most remarkable 3D PBG architectures is the square spiral consisting of solid posts connecting roughly the nearest neighbor points of the diamond lattice. As we show below, this achieves a very large waveguide bandwidth with a relatively modest 3D PBG cladding. This 3D PBG crystal has already been successfully synthesized using glancing angle deposition (GLAD) techniques [18]. The optimized [001]-diamond:1 structure is characterized by $[L, c, r] = [0.70, 1.35, 0.20]a$, corresponding to a dielectric volume fraction of $\sim 31\%$. This structure possesses a 3D PBG of $\sim 14.8\%$. We scan the structural parameters r from $0.16a$ to $0.24a$ and t from $0.3a$ to $0.8a$ and calculate the waveguiding bandwidth for each case. The results are summarized in Fig. 13. The largest waveguiding bandwidth of ~ 185 nm is obtained when $t = 0.55a$ and $r = 0.16a$. The dispersion relation in this case is shown in Fig. 14. It is worth noting that this structure exhibits stronger tolerance on the thickness disorder than the previous structures, as we can see that the waveguiding bandwidth remains larger than 175 nm for a wide range of parameters r and t .

D. Inverse [001]-diamond:1

Finally, we consider the inverse [001]-diamond:1 with the optimal structural parameters $[L, c, r] = [0.45, 1.43, 0.395]a$. The dielectric volume fraction is $\sim 19\%$ and the size of 3D PBG is $\sim 22\%$ in this case. Figure 15 shows the waveguide bandwidth for r varied from $0.11a$ to $0.17a$ and t varied from $0.3a$ to $0.8a$. The maximum waveguiding bandwidth of ~ 184 nm is obtained when $t = 0.5a$ and $r = 0.13a$. We show the dispersion relation of the waveguide mode for the optimal case in Fig. 16. Clearly, a single waveguide mode spanning most of the entire on-chip band gap is achieved. Note that in Figs. 14 and 16, although the waveguiding bandwidth may seem likely to increase by increasing the thickness of the 2D PC layer, our calculation shows that it does not. In the case of thicker t , the dispersion line of the waveguide mode bends toward the lower frequency at the wave vector near

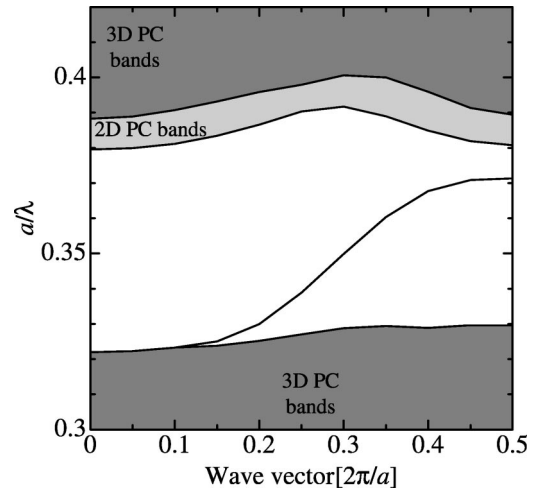


FIG. 14. Dispersion relation for an air waveguide channel in the [001]-diamond:1 square spiral based heterostructure. The thickness of 2D PC layer is $0.55a$ and the radius of rod in the 2D PC layer is $0.16a$.

$k = 0.45[2\pi/a]$, leading to no increase in the single-mode waveguiding bandwidth. We also note that in each of the examples above, our waveguide bandwidth optimization procedure has been restricted to simply removing a single row of dielectric rods on the microchip layer. It is possible that even greater bandwidth for single-mode propagation may be achieved by additional adjustment of the radius of rods alongside the waveguide channel [34].

V. WOODPILE STRUCTURES

In this section, we briefly describe the 2D-3D heterostructure based on the woodpile structures [6,10,19,20] and a matching square lattice 2D PC slab. Figure 17 shows a schematic of the woodpile based heterostructure. For concreteness, we consider a woodpile structure that consists of stacking rods with a rectangular cross section. The width and height of rods are $0.25a$ and $0.3a$, respectively, where a is a

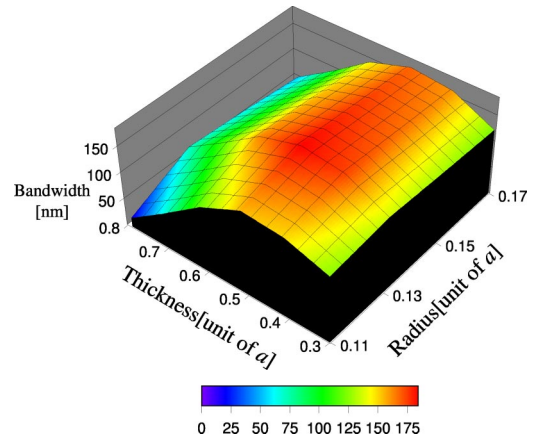


FIG. 15. Waveguiding bandwidth as a function of the thickness of 2D PC layer and the radius of rod in the 2D PC layer for the inverse [001]-diamond:1 square spiral based heterostructure.

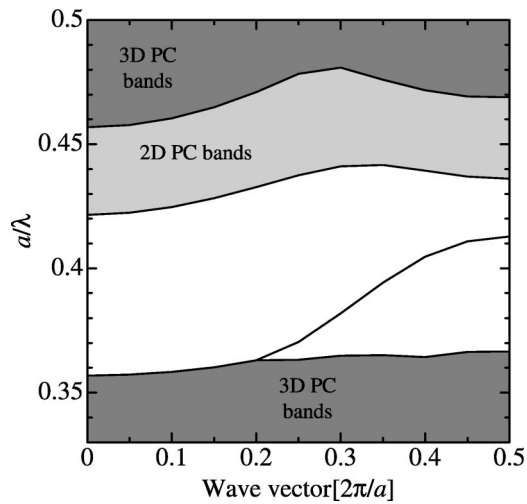


FIG. 16. Dispersion relation for an air waveguide channel in the inverse [001]-diamond:1 square spiral based heterostructure. The thickness of 2D PC layer is $0.5a$ and the radius of rod in the 2D PC layer is $0.13a$.

distance between two adjacent rods in the same layer. One unit cell of the woodpile consists of four stacking layers. Accordingly, the periodicity in the stacking layer is $1.2a$. Calculation of the band structure by the PW method reveals that this woodpile structure exhibits a 3D PBG of $\sim 17.7\%$. We start by considering the embedding position. We choose to insert the 2D PC layer in between a pair of adjacent layers of the woodpile. This embedding position is a natural one for layer-by-layer fabrication. Moreover, this position is expected to yield a large on-chip band gap by way of analogy

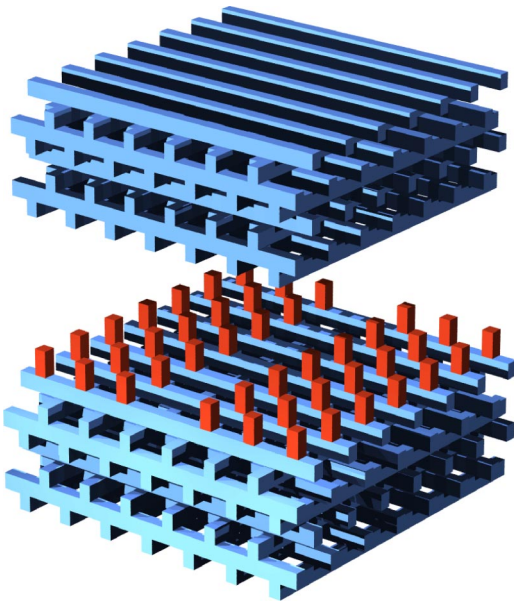


FIG. 17. Schematic of the woodpile based heterostructure. The 2D PC layer consisting of a square lattice of square rods is placed on top of the lower woodpile 3D PBG cladding layer. A linear waveguide (missing row of rods) is depicted in the 2D PC layer. The upper 3D PBG cladding layer is separated to help visualize the 2D PC layer.

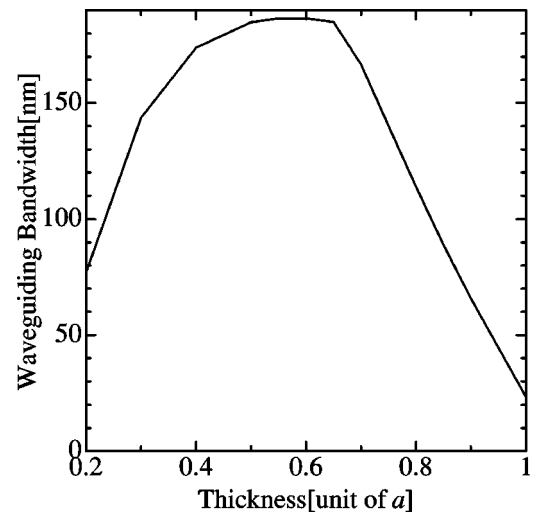


FIG. 18. Waveguiding bandwidth as a function of the thickness of 2D PC layer for the woodpile based heterostructure. The width and thickness of woodpile rods are $0.25a$ and $0.3a$, respectively. The width of square dielectric rods in the 2D PC layer is also $0.25a$.

to the elbow positions in the square spiral structure. In particular, the elbows may be regarded as the equivalent points of intersection. Indeed, our calculation confirms that this embedding position provides the largest on-chip band gaps. For the 2D PC layer, a square lattice of square dielectric rods with width of $0.25a$ is chosen to structurally match with the woodpile structure. One rod is placed at each of the square lattice points defined by crossing points of the adjacent woodpile layers.

An air waveguide is created by removing a row of dielectric rods in the 2D PC layer. Since the width of square rods in the 2D PC layer is already determined, we only need to consider the thickness of the 2D PC layer with respect to the waveguiding bandwidth. We show in Fig. 18 a plot of single-mode waveguiding bandwidth as a function of the thickness and in Fig. 19, the dispersion relation of the waveguide when $t=0.8a$. The optimized waveguiding bandwidth of ~ 186 nm is obtained when $t=0.55a$.

To demonstrate the diffractionless propagation of light inside the heterostructure, we use the 3D FDTD to calculate the transmission and reflection spectra for the waveguide bend in the woodpile-based heterostructure with $t=0.8a$. By choosing $t=0.8a$, we obtain a relatively small-dispersion waveguide mode with a group velocity of $\sim 0.265c_0$, which covers the entire on-chip band gap of roughly 90 nm. The FDTD results show that the transmission is $>99\%$ for almost the entire band gap and the reflection is $<0.3\%$ for the same range. This is in contrast with the previously reported waveguide bend using two layers in the woodpile structure [6–8] where there exists reflection of up to 5% over the spectral range of ~ 145 nm. Figure 20 shows a snap shot of the electromagnetic pulse propagating along the waveguide bend and the inset shows the transmission and reflection spectra. The field pattern is shown for the z component of the electric field at the center of the 2D PC layer. To further illustrate the lossless flow of light on the microchip layer, we consider a single-defect cavity displaced by $2a$ from the air waveguide

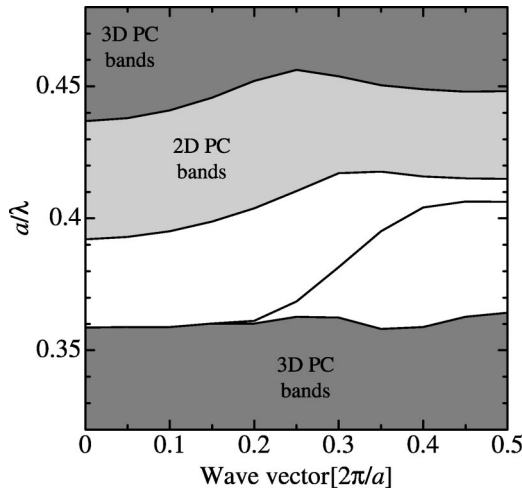


FIG. 19. Dispersion relation for an air waveguide channel in the woodpile based heterostructure. The thickness of 2D PC layer is $0.8a$.

as shown in Fig. 21(a). In addition, we adjust the quality factor of the cavity mode by reducing the dielectric constant of the intervening rod. This is to reduce the interaction time between the waveguide and resonator in our computations. The transmission and reflection spectra shown in Fig. 21(b) clearly indicate the $\sim 100\%$ reflection at the resonant frequency of $a/\lambda=0.382$. Unlike the corresponding result for the 2D PC slab with a uniform medium above and below, in our 2D-3D PBG heterostructure, there is no leakage of light into the third dimension. The oscillation seen in the transmission spectrum is an artifact of the computational method [4,6,35,36].

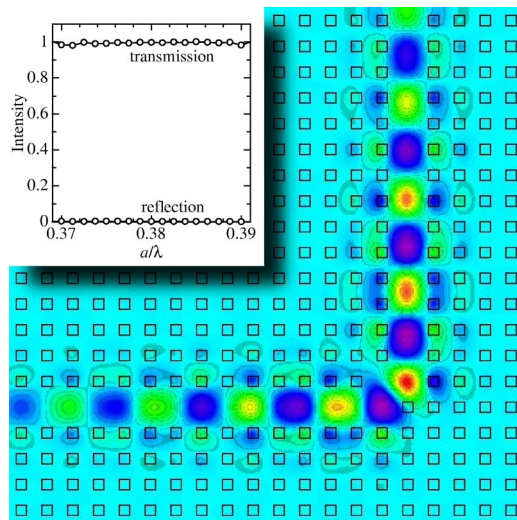


FIG. 20. Electric field pattern in the vicinity of the waveguide bend as an electromagnetic pulse propagates along the waveguide bend. The field pattern is shown for the z component of the electric field at the center of the 2D PC layer. The inset shows the transmission and reflection spectra of the waveguide bend. The transmission is over 99% for almost the entire on-chip band gap.

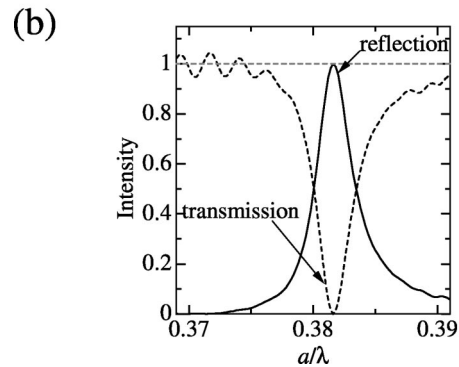
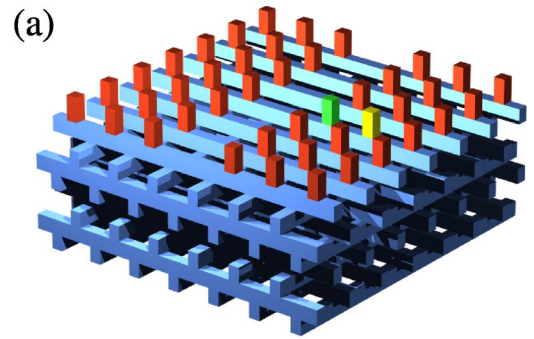


FIG. 21. (a) Schematic of the waveguide-defect cavity system inside the woodpile based heterostructure. A single-defect cavity is created by changing the dielectric constant of one rod in the vicinity of the waveguide from 11.9 to 2.09 ($2a$ from the waveguide). The dielectric constant of the adjacent rod (also adjacent to the waveguide) is adjusted to 6.45 for computational convenience. (b) Transmission and reflection spectra for the system in (a) calculated by 3D FDTD.

VI. SLANTED PORE STRUCTURES

In this section, we describe in detail the 2D-3D heterostructure appropriate to the recently discussed slanted pore 3D PBG architectures [21]. We consider only the simplest slanted pore PBG architectures [21] which we denote as (a) SP_2 and (b) SP_3 . They are fabricated by drilling 2 slanted pores in each unit cell of the square lattice SP_2 or 3 slanted pores in each unit cell of the triangular lattice SP_3 . One class of SP_3 structures (sometimes called Yablonoivite) was among the first PBG materials fabricated with a 3D PBG in the microwave spectrum [22].

A. SP_2 -based heterostructures

The SP_2 photonic crystals are defined by a tetragonal lattice with lattice constants c along the z axis and a along the x and y axes. One unit cell consists of two cylindrical pores of radius r aligned in the (a, a, c) and $(-a, -a, c)$ directions. These two pores are displaced in the x direction by $0.5a$. The optimized SP_2 structure we use here has the structural parameters $c=1.40a$ and $r=0.345a$ and exhibits a complete PBG of $\sim 24\%$ [21]. The dielectric volume fraction is approximately 20%. Figure 22 shows a schematic of the slanted pore structure based heterostructure.

To consider the embedding position, we show a unit cell of the SP_2 structure in Fig. 23. Observably, the structure

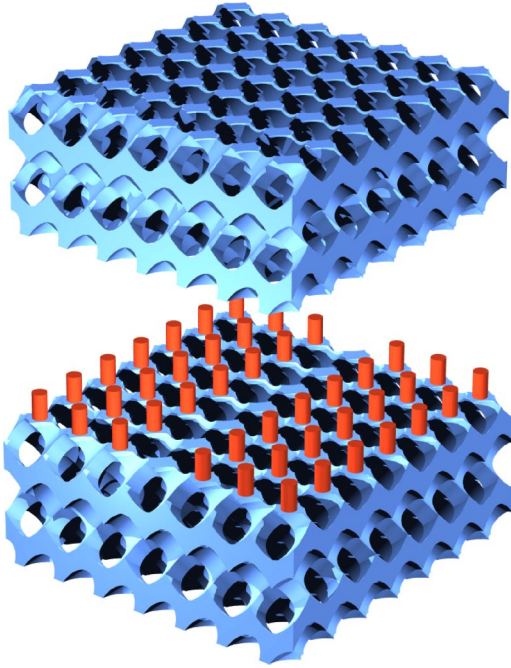


FIG. 22. Schematic of the SP_2 based heterostructure. The 2D PC layer consisting of a square lattice of circular rods is placed on top of the lower SP_2 3D PBG cladding layer. A linear waveguide (missing row of rods) is depicted in the 2D PC layer. The upper 3D PBG cladding layer is separated to help visualize the 2D PC layer.

exhibits a spiralling feature. By analogy to the square spiral PBG material, it is suggestive that we choose the embedding position at the “elbow” of the spiral feature. This corresponds to the position $z=1/8c$. It is noticeable that in fact the cross-section of the SP_2 structure at this embedding position represents a square lattice of isolated dielectric islands (see Fig. 22). This structurally matches with the 2D PC layer, which is a square lattice of circular dielectric rods. This is also true the square spiral structure. This further suggests that resemblance of the cross section to the chosen 2D PC layer may serve as a rule of thumb for selection of the embedding position. A square lattice of circular dielectric rods with radius $r=0.15a$ and thickness $t=0.6a$ is assumed for the 2D PC layer. One rod is placed at each of the square lattice points defined by the center of dielectric islands visible at the cross section.

We create the air waveguide by removing a row of dielectric rods in the 2D PC layer. The dispersion relation of the waveguide mode for $t=0.6a$ is calculated by the PW method and shown in Fig. 24. The single-mode, air waveguiding bandwidth is approximately 180 nm in this case and remains well above 165 nm throughout the range $0.4a \leq t \leq 0.65a$.

B. SP_3 -based heterostructures

We illustrate the heterostructure structure based on the SP_3 -Yablonovite structure with an intercalated triangular lattice of dielectric rods forming the microchip layer. The SP_3 structure can be fabricated by drilling holes through a triangular lattice mask in three directions at an angle 35.26° away from normal and spread out 120° on azimuth, for each lattice

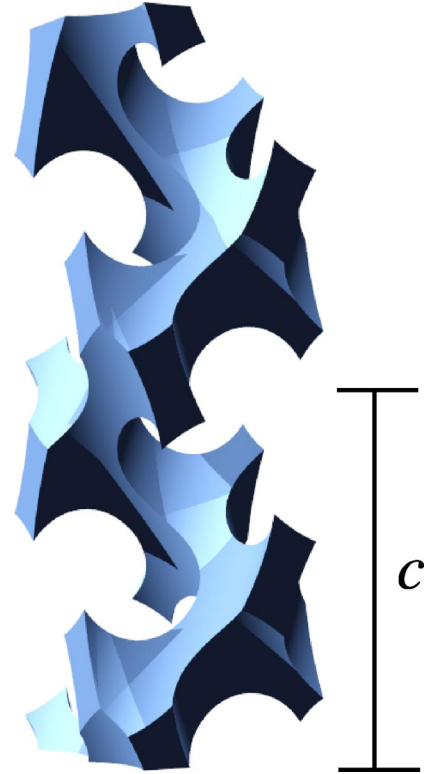


FIG. 23. Schematic showing two unit cells of the SP_2 structure. The structural parameters are $c=1.40a$ and $r=0.345a$.

point of the triangular lattice [22]. The drilled structure forms an fcc lattice with its surface parallel to the (111) plane. We employ the SP_3 structure with the following structural parameters: the radius of air cylinders $r=0.3a$, where a is $1/\sqrt{2}$ times the lattice constant of the fcc lattice. The structure consists of roughly 31% of dielectric and 69% of air. The size of the 3D PBG is $\sim 15\%$. Here, we employ the principle (suggested in the previous section) that the cross section of the Yablonovite structure at the embedding position should

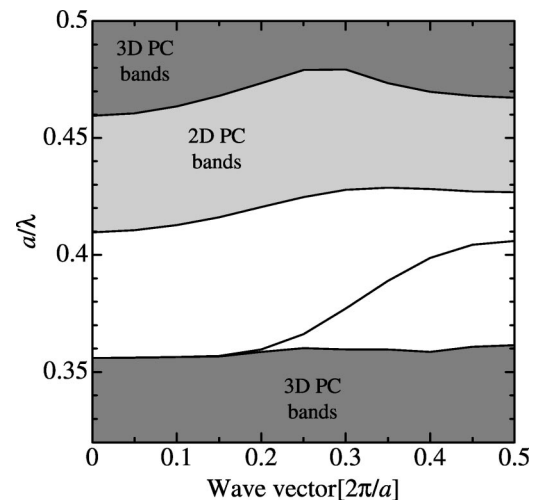


FIG. 24. Dispersion relation for an air waveguide channel in the SP_2 based heterostructure. The thickness of 2D PC layer is $0.6a$ and the radius of rod in the 2D PC layer is $0.15a$.

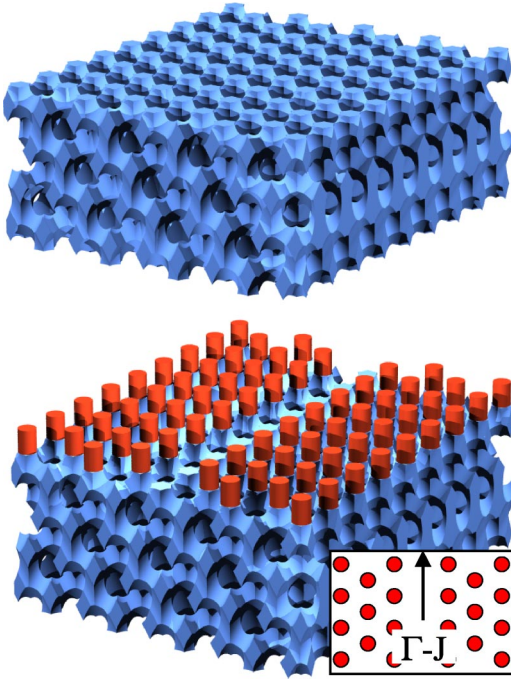


FIG. 25. Schematic of the Yablonovite based heterostructure. The 2D PC layer consisting of a triangular lattice of circular rods is placed on top of the lower Yablonovite 3D PBG cladding layer. A linear waveguide (missing row of rods) is depicted in the 2D PC layer. The upper 3D PBG cladding layer is separated to help visualize the 2D PC layer. An inset describes the crystalline direction Γ - J .

represent a triangular lattice of dielectric rods. This corresponds to the positions $z=1/6c$, $3/6c$, or $5/6c$ below the surface at which all three pores coincide, where c is $\sqrt{6}a$. A layer of dielectric rods with radius $r=0.2a$ and thickness $t=0.4a$ is embedded at such position and one row of rods in the Γ - J direction (see Fig. 25 inset) is removed to create a waveguide. Figure 25 illustrates the heterostructure based on the Yablonovite structure. We show in Fig. 26 the band structure of the air waveguide inside the Yablonovite based heterostructure. Clearly, a single-mode waveguide that spans the entire on-chip band gap of approximately 160 nm is successfully obtained.

VII. INVERSE OPAL STRUCTURES

As a final illustration of a 2D-3D PBG heterostructure, we consider the inverse opal structure. In order to obtain the maximum bandwidth for embedded optical circuitry, we employ the inverse opal cladding structure reported in Ref. [24]. The structure contains closed-packed air spheres ($r=0.5a$, where a is a distance between the center of two adjacent spheres) surrounded by spherical shells (radius $1.25r$) and connected by cylindrical windows (radius $0.4r$). The volume fraction of dielectric materials is approximately 21%. Our calculation shows that there exists a PBG of $\sim 11.2\%$ in a normalized frequency range $a/\lambda=0.583-0.653$. We choose to cut the inverse opal structure at the (111) plane, since in real fabrication processes, the opal spheres are stacked along

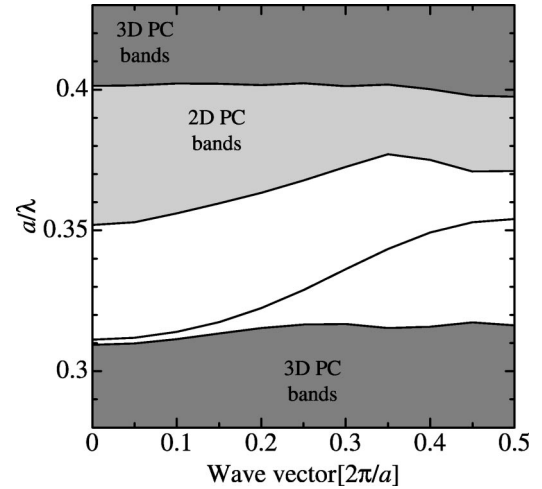


FIG. 26. Dispersion relation for an air waveguide channel in the Yablonovite based heterostructure. The Yablonovite structure with radius of air cylinder $r=0.3a$, where a is $1/\sqrt{2}$ times the lattice constant of the fcc lattice is used. The thickness of 2D PC layer is $0.4a$ and the radius of rod in the 2D PC layer is $0.2a$.

the [111] direction [25]. The 2D photonic crystal slab must then be a triangular lattice, in order to match the (111) plane of the inverse opal structure.

In practice, this heterostructure can be fabricated in one of two ways. The first is by infiltrating the opal template with silicon and overgrowing a silicon slab layer of prescribed thickness above the top surface of the silicon-silica composite, during the silicon chemical vapour deposition (CVD) process. This silicon slab surface is then polished and patterned as a 2D photonic crystal with a triangular lattice of holes and circuitry (missing holes). This patterning step may be done by electron-beam lithography, where it has been shown that accurate alignment of this patterning with the underlying photonic crystal is achievable [20]. An alternative alignment method using laser beam diffraction developed by Noda *et al.* [37] is also available and very high precision in alignment has been achieved [10]. The holes are then filled using silica CVD and the surface is polished once again. The upper cladding layer can then be created by depositing an opal template on top of the solid microchip slab layer, applying silicon CVD to the upper layer, and finally removing silica throughout the heterostructure by wet chemical etching [25]. This approach provides a microchip consisting of air holes in a silicon membrane.

An alternative microchip architecture may be realized by CVD of silicon into the lower silica opal template section, either up to or below the top of the silica spheres in the uppermost layer of spheres. After this, silica CVD is performed to create a solid slab of silica of desired thickness on top of the silicon-silica composite structure described above. The exposed silica surface is then polished. This silica membrane is patterned as a 2D photonic crystal with a triangular lattice of holes and circuitry (missing holes). The holes of the silica membrane (that sits on top of the previously infiltrated silicon-silica composite below) are then filled using silicon CVD and the exposed surface is polished. The upper cladding layer is created as in the previous case and finally silica

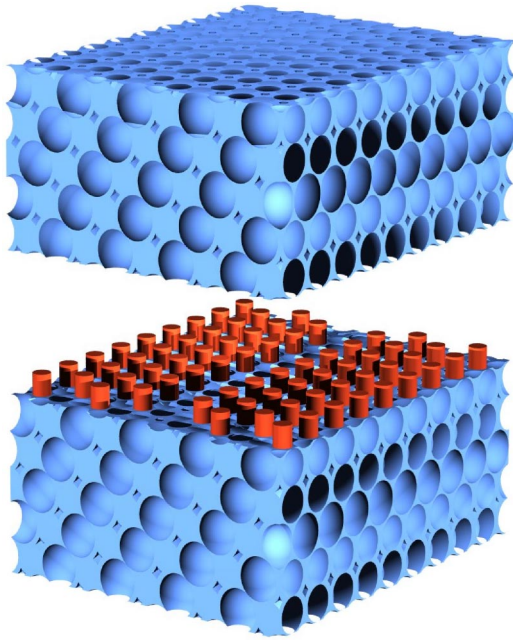


FIG. 27. Schematic of the inverse opal based heterostructure. The 2D PC layer consisting of a triangular lattice of circular rods is placed on top of the lower inverse opal 3D PBG cladding layer. A linear waveguide (missing a row of rods) is depicted in the 2D PC layer. The upper 3D PBG cladding layer is separated to help visualize the 2D PC layer.

is removed from the entire heterostructure by wet chemical etching. This second approach provides a micro-chip consisting of silicon rods in air background (see Fig. 27).

In the first heterostructure, waveguides consist of columns of solid silicon in the micro-chip layer, whereas in the latter heterostructure we obtain air waveguides in a triangular lattice of silicon rods. As discussed in Sec. II, here we choose to concentrate on the latter.

Figure 27 shows a schematic of the heterostructure based on the inverse opal 3D PBG with an intercalated triangular lattice microchip of dielectric rods in an air background. First, we consider the embedding position. Figure 28(a) shows a side view of the inverse opal structure, where the z axis is parallel to the $[111]$ direction. The lattice constant along the $[111]$ direction is c . There are three equidistant planes in one period of the structure, namely A, B, and C, respectively. Since these planes are symmetrically equivalent, it is adequate to consider the embedding position within the range of $z=0$ to $z=1/6c$. We show in Figs. 28(b)–28(f) cross sections of the inverse opal structure at the planes $z=0$, $z=1/24c$, $z=1/12c$, $z=1/8c$, and $z=1/6c$, respectively. Clearly, the structures in Figs. 28(b)–28(f) are quite distinct. While Figs. 28(b) and 28(c) represent disconnected dielectric rods in air background in a hexagonal lattice, Figs. 28(d) and 28(e) show a triangular lattice of air rods in dielectric background. Figure 28(f) shows a triangular lattice of hollow-core dielectric rods in air background. For compatibility with a 2D photonic crystal layer consisting of a triangular lattice of dielectric rods in air background, we choose to place the bottom surface of the 2D microchip layer at $z=1/6c$ (or half the way between two spheres). In this manner the cross sec-

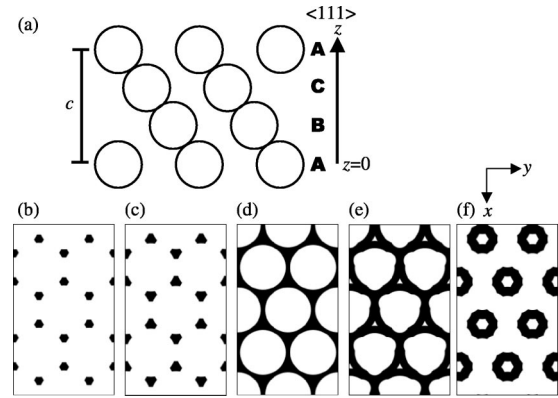


FIG. 28. Schematic showing the inverse opal structure. The opal spheres are assumed stacking along the $\langle 111 \rangle$ direction. (a) Side view of the inverse opal structure showing three equivalent planes, namely A, B, and C. (b)–(f) Cross sections of the inverse opal structure at the planes $z=0$, $z=1/24c$, $z=1/12c$, $z=1/8c$, and $z=1/6c$, respectively.

tions of inverse opal structure and 2D photonic crystal layer match each other. The 2D photonic crystal layers is inserted in a manner that each dielectric rod is centered at the center of the corresponding hollow-core dielectric rod visible at the cross section of the inverse opal PBG. We note here that the inner and outer radii of the hollow-core dielectric rods are approximately $0.12a$ and $0.28a$, respectively.

We consider an air waveguide inside the heterostructure created by removing one row of dielectric rods in the Γ - J direction of the triangular lattice (or the y direction as indicated in Fig. 28). We show the dispersion relation of the waveguide mode for the case that $r=0.22a$ and $t=0.15a$ in Fig. 29. We can clearly see a single waveguide mode spanning a large fraction of the on-chip band gap from $a/\lambda = 0.586$ – 0.616 .

We scan the structural parameters r from $0.18a$ to $0.28a$ and t from $0.1a$ to $0.2a$ and calculate the waveguiding bandwidth for each case. The results are summarized in Fig. 30. We find that the largest waveguiding bandwidth of ~ 74 nm is obtained when the thickness is $t=0.15a$. The dependence of the waveguiding bandwidth to the radius r is relatively small in the range shown in Fig. 30.

Finally, we summarize in Table I the results for all of the 2D-3D heterostructures considered in Secs. IV–VII. It is interesting to note that the maximal bandwidth of the single-mode air waveguide is roughly 180 nm for a number of different 3D PBG cladding, while the complete PBG of these structures differ by considerably. For the 3D structures with a large PBG, the 2D PC slab modes emerge quickly as the thickness of 2D PC layer increases. This destroys large parts of the PBG and leaves ~ 180 nm of bandwidth for the air waveguide channel (for example, see Fig. 10). On the other hand, for the 3D structures with a smaller PBG, the appearance of 2D PC slab modes is slower and a smaller part of the PBG is spoiled. Finally, this again leaves ~ 180 nm of bandwidth for the air waveguide channel (for example, see Fig. 14).

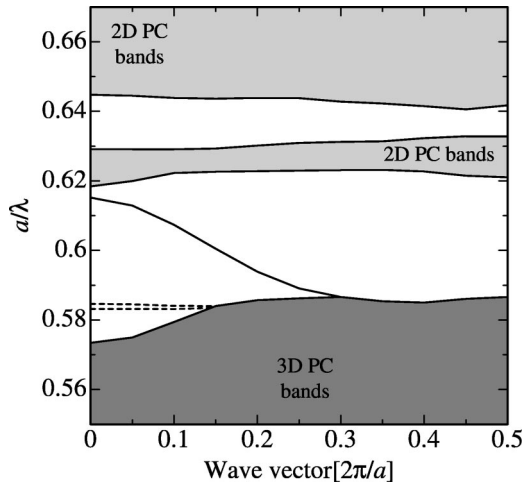


FIG. 29. Dispersion relation for an air waveguide channel in the inverse opal based heterostructure. The thickness of 2D PC layer is $0.15a$ and the radius of rod in the 2D PC layer is $0.22a$. The PC layer is $0.8a$.

VIII. EFFECTS OF STRUCTURAL DISORDERS

From a practical point of view, it is important to examine the robustness of the heterostructures described above to small changes in the geometry of the structures. For illustrative purposes, we study the effect of structural disorders in the inverse [001]-diamond:5 square spiral-based heterostructures. We may classify the disorders effects in the inverse square spiral-based heterostructure into two categories: the first one related only to the square spiral itself and the second one related to the 2D PC layer. Since the disorder effects in the square spiral PBGs have been reported elsewhere [17], here we consider only the disorders related to the 2D PC layer.

First, we consider small random variations in the parameters r (radius of rods in the 2D PC layer) and t (thickness of the 2D PC layer) that are likely to occur from point to point within the photonic crystal heterostructure. The useful waveguiding bandwidth in a weakly disordered heterostructure may then be estimated by the intersection of the various waveguiding bands obtained from the set of perfect heterostructures which sample the distribution of parameters r and t . A more direct measure of backscattering loss in a true

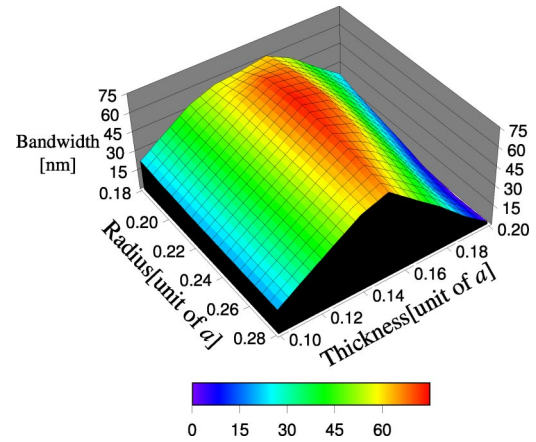


FIG. 30. Waveguiding bandwidth as a function of the thickness of 2D PC layer and the radius of rod in the 2D PC layer for the inverse opal based heterostructure.

disordered system will be presented using FDTD at the end of this section. Figure 31 shows the change in the position of the lower and upper edges of the waveguiding frequency band as a function of the change in r and t . The frequencies of the band edges are plotted against the relative change in the above parameters. The initial structure corresponds to the inverse square spiral based heterostructure with $t=0.45a$ and $r=0.17a$. Clearly, an error in the thickness t has a more deleterious effect than a comparable error in the radius r .

Second, the effect of transverse misalignment between the 2D PC layer and the inverse [001]-diamond:5 square spiral is examined. For simplicity, we assume that the 2D photonic crystal is registered with the lower inverse square spiral cladding layer. The upper layer is then assumed shifted (misplaced) from its designed position by the distance of Δ in either the x or y direction. Here, the x and y direction refer to the waveguiding direction and the perpendicular direction, respectively, and the z direction is normal to the microchip layer. We calculate the band structures for various Δ for both the shift in the x and y direction and show the results in Fig. 32. The results reveal that the single-mode waveguiding bandwidth of the heterostructure remains larger than 142 nm and 160 nm for the shift of up to 100 nm (or $\sim 0.18a$) in the x and y directions, respectively. The single-mode waveguiding bandwidth vanishes when the shift is larger than

TABLE I. Summary of the optimized heterostructures for different types of 3D PBG cladding.

3D structure	Size of PBG of 3D cladding	2D lattice structure	Optimized single-mode waveguide bandwidth (nm)	Thickness of 2D layer
Direct [001]-diamond:5 spiral	16%	square	155	$0.5a$
Inverse [001]-diamond:5 spiral	23%	square	183	$0.45a$
Direct [001]-diamond:1 spiral	15%	square	185	$0.55a$
Inverse [001]-diamond:1 spiral	22%	square	184	$0.5a$
Woodpile	18%	square	186	$0.55a$
SP ₂	24%	square	180	$0.6a$
SP ₃ (Yablonovite)	15%	triangular	160	$0.4a$
Inverse opal [111]	11%	triangular	74	$0.15a$

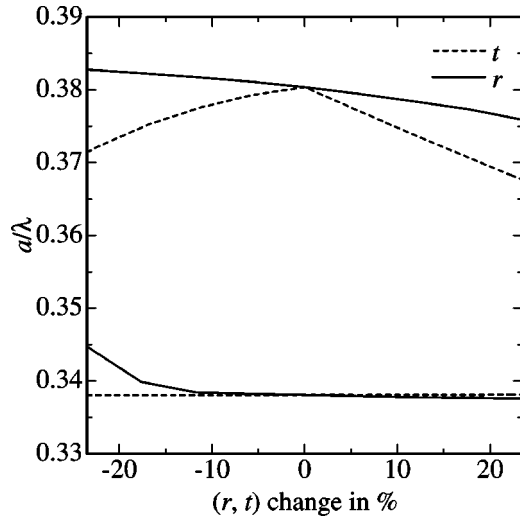


FIG. 31. Waveguiding band edges of the waveguide in the inverse square spiral based heterostructure as a function of change in the geometry of the 2D PC layer. The relative change in t and r are measured in percentage. The initial geometry corresponds to $t = 0.45a$ and $r = 0.17a$.

~ 200 nm for the x direction and ~ 250 nm for the y direction. Our studies suggests the following general rules of thumb: (i) Transverse misalignment by 80 nm has almost no deleterious effect on the single-mode waveguiding bandwidth; (ii) the heterostructure can withstand roughly 150 nm of misalignment before losing a major part of its functionality.

The analysis above focussed on the effect of structural variations on the overall spectral window of single-mode waveguiding. Clearly these variations reduce the available window. However, even within the reduced windows, disorder can lead to optical backscattering losses along the air-

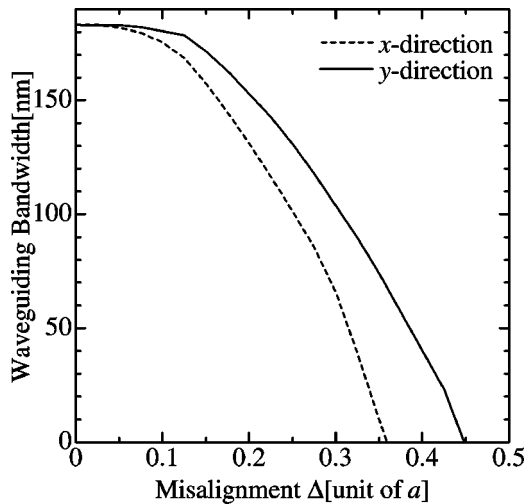


FIG. 32. Waveguiding bandwidth of the waveguide in the inverse square spiral based heterostructure as a function of misalignment between the 2D PC layer and the upper 3D PBG cladding. The x and y directions correspond to the waveguiding direction and the perpendicular direction, respectively. The parameters of the heterostructure are $t = 0.45a$ and $r = 0.17a$.

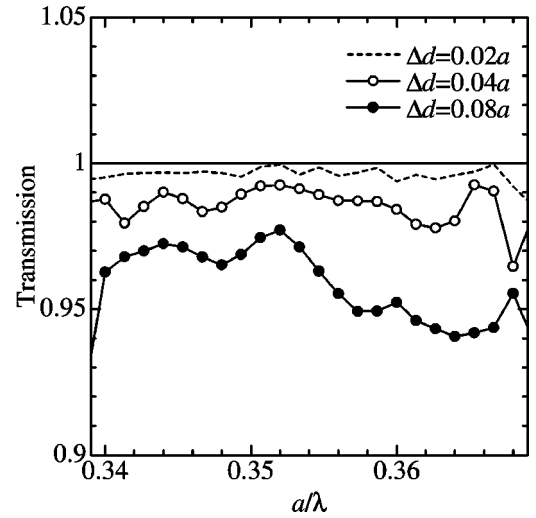


FIG. 33. Transmission spectra for electromagnetic waves propagating through a distance of 20 unit cells in disordered waveguides in the inverse [001]-diamond:5 square spiral based heterostructure. Each line represents an averaged result of 10 configurations of randomly disordered waveguide.

waveguiding channel. We investigate these backscattering losses by the FDTD simulations. An air waveguide is created by removing a row of dielectric rods in a disordered inverse [001]-diamond:5 heterostructure with $t = 0.5a$. Dielectric rods with different diameters ranging from $d = (0.34 - \Delta d)a$ to $(0.34 + \Delta d)a$ are randomly distributed in the 2D PC layer. The number of rods possessing a certain radius forms a uniform distribution with an average $d = 0.34a$. We consider three cases of disorders, namely, $\Delta d = 0.02, 0.04,$ and $0.08a$. (For a microchip operating at wavelengths near 1.5 microns, this corresponds to $\Delta d \sim 12, 24,$ and 48 nm, respectively.) The transmission coefficients of electromagnetic waves propagating through a distance of 20 unit cells across the disordered waveguide are shown in Fig. 33. The broken line, open-circle line, and solid-circle line correspond to $\Delta d = 0.02, 0.04,$ and $0.08a$, respectively. The solid line at transmission equal to one is a guide to the eyes. Figure 33 represents the averaged result of 10 configurations of randomly disordered waveguide. It is seen that the transmission is reduced by $\sim 1-2\%$ (or $\sim 0.0036-0.0072$ dB/ μm) for a disorder of ~ 24 nm. The averages of the reflection coefficients over a range of frequency $a/\lambda = 0.341-0.367$ are 0.32%, 1.34% and 4.04% for $\Delta d = 0.02, 0.04,$ and $0.08a$, respectively. Although more numerical data are required for a solid conclusion, we find that the reflection coefficients roughly follow the quadratic function of Δd , as appropriate for a 1D Rayleigh scattering mechanism.

Finally we note that diffractionless flow of light in our 2D-3D PBG heterostructure, with disorder, is considerably more robust than waveguiding in a solid waveguide through a 2D PC membrane with uniform dielectric (say air) above and below. In the latter case, significant small angle forward scattering can lead to leakage of light into the third dimension (normal to the membrane) [38,39]. In the 2D-3D PBG microchip, all “final states” with a vertical wave-vector component, that light could even “in principle” scatter into, have

been removed by virtue of the on-chip 3D PBG.

IX. 2D-1D HETEROSTRUCTURES

It is tempting to ask whether other cladding materials above and below a 2D microchip might also be effective in preventing diffractive loss into the third dimension. In order to address this question, we provide a comparison between the heterostructures using 3D PBG materials as cladding layers and a hypothetical heterostructure using 1D PC omnireflectors [26,27] as cladding layers. Omnireflectors consisting of 1D multilayer stacks have been shown to reflect plane waves impinging from any angle onto their surface under idealized conditions. Earlier, a theoretical analysis on the 2D-1D heterostructures or the heterostructures using 1D PC omnireflectors as cladding layers has been reported [40]. However, the analysis employed a simplified model that assumes only 1D omnireflectors with a thin layer of air waveguide and does not really include the 2D PC layer. This has led to an overly optimistic result on the confinement of light. In contrast, we present here a 3D analysis of the 2D-1D heterostructure based on the 3D FDTD methods.

We begin by discussing the types of confinement of light inside the waveguide created by removing a row of dielectric rods in the 2D photonic crystal layer. It is important to emphasize here that it is not possible to obtain a complete confinement of light inside such a waveguide since the light inside the waveguide acts as a point source very near to the surface of the omnireflector. Moreover, the evanescent field of the air waveguide penetrates into the interior of the omnireflector. Consequently, light from the waveguide will couple to the propagating modes of the omnireflector unlike the light from a source far away from the omnireflector surface [26]. Therefore, our aim here is not simply to disprove complete confinement, but rather to evaluate the strength of confinement of the 2D-1D heterostructure waveguide or equivalently, the leakiness of the waveguide.

Figure 34 shows a schematic of the 2D-1D heterostructure. We assume the 1D omnireflectors with the same structural parameters as in [40], that is, one unit cell of the 1D omnireflector consists of GaAs ($n=3.5$) with thickness d_1 and oxidized AlAs ($n=1.56$) with thickness d_2 . The 1D lattice constant $c=d_1+d_2$ and we choose the ratio $d_2/d_1=2$. The thickness of the 2D photonic crystal layer is assumed equal to d_2 . The model in [40] was only one-dimensional and did not include the 2D photonic crystal. In our model, we choose the intercalating 2D PC lattice to have a lattice constant $a=1.5c$ in order to obtain overlap between the 2D PBG and the 1D omnireflection spectral range. The omnireflecting frequency range for the multilayer stacks above is approximately from $c/\lambda=0.17-0.28$. An idealized 2D square lattice of infinitely long dielectric rods with radius of $0.2a$ in an air background provides an in-plane band gap for the similar frequency range of $a/\lambda=0.28-0.42$.

First, we employ the 3D FDTD method with the Bloch boundary condition in the waveguiding direction and the periodic boundary conditions in the other two directions to estimate the frequency and dispersion relation of the waveguide mode. By using periodic boundary conditions, the air

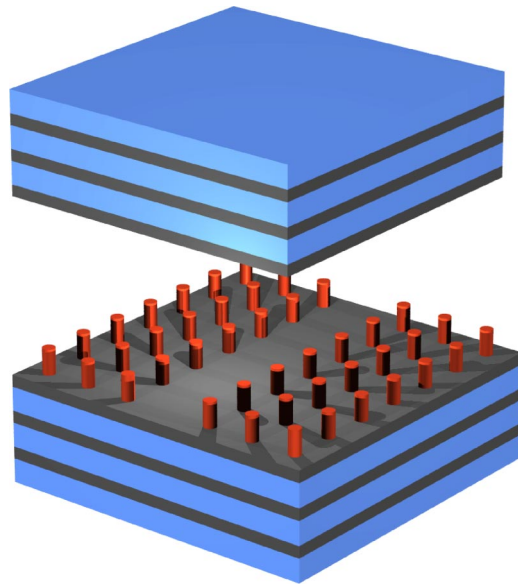


FIG. 34. Schematic of the 2D-1D heterostructure. The 2D PC layer consisting of a square lattice of circular rods is placed on top of the lower 1D omnireflector cladding layer. The dark and light layers correspond to materials with higher and lower dielectric constants, respectively. A linear waveguide (missing row of rods) is depicted in the 2D PC layer. The upper 1D omnireflector cladding layer is separated to help visualize the 2D PC layer.

waveguide mode is completely confined and nonleaky, thus facilitating identification of the air waveguide mode. We assume a supercell consisting of 5 dielectric rods on either side of the waveguide in the 2D PC layer and 5 unit cells of the 1D omnireflector layers on each side (top and bottom) of the 2D PC layer. Shown in Figs. 35(a) is the dispersion relation of the TM-like waveguide mode, which spans the frequency range $a/\lambda=0.28-0.37$ as expected. Figure 35(b) shows the field pattern in the vertical cross section for the wave vector $0.2 [2\pi/a]$. Second, we assume the Mur's second order absorbing boundary condition (ABC) in the vertical direction instead of the periodic boundary conditions to allow leakage of light from the heterostructure. These ABCs simulate semi-infinite stacks of GaAs cladding on top and bottom of the 2D-1D heterostructure and allow the light leaked to be absorbed without being reflected back into the heterostructure.

The propagation loss of the waveguide can be found by calculating the quality factor (Q) of the waveguide mode [41]. The transmission coefficient after propagating the length L for particular angular frequency ω is equal to $\exp(-L\omega/Qv_g)$, where v_g is the group velocity of the waveguide mode at ω . The Q factor of the waveguide mode is calculated by measuring the ratio of the total power inside the heterostructure and the power absorbed by the ABCs. We find that the propagation loss for the wave vector $0.2 [2\pi/a]$ (or $a/\lambda \sim 0.306$) is on the order of $\sim 2 \text{ dB}/\mu\text{m}$ for light at 1.5 microns. Clearly, the 2D-1D heterostructure with 5 unit cells of 1D omnireflectors on each side is extremely ineffective in confining light in the waveguide. Since the waveguide mode excites propagating modes of the 1D omnireflector, increasing the thickness of the cladding does not improve matters. This is in a

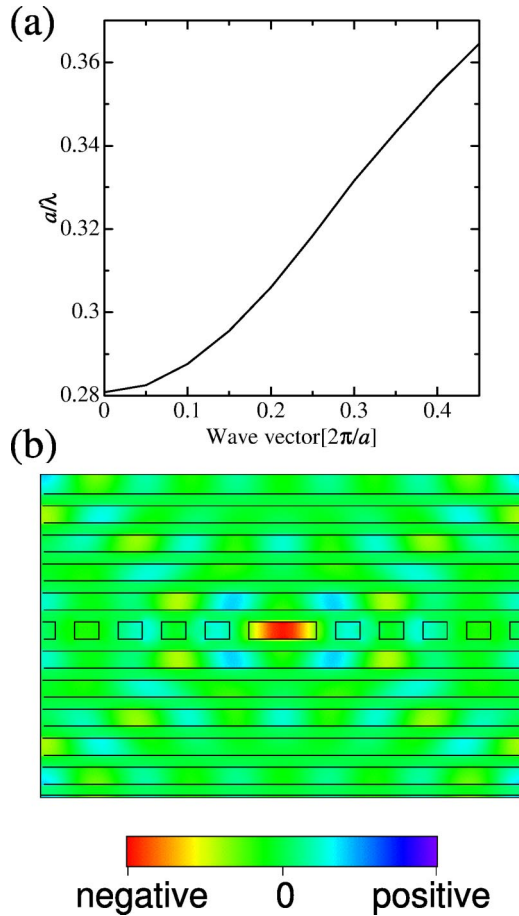


FIG. 35. (a) Dispersion relation for the fundamental TM-like mode of air waveguide channel in the 2D-1D heterostructure. The thickness of 2D PC layer is $0.44a$ and the radius of rod in the 2D PC layer is $0.2a$. (b) Distribution of the electric field for the waveguide mode at the vertical cross section that cuts through the center of dielectric rods. The wave vector is $0.2 [2\pi/a]$.

strong contrast with the 2D-3D heterostructure where the confinement is better than 10^{-5} dB/ μm for five unit cells of the 3D PBG cladding material. Moreover, for the 3D PBG cladding, the confinement improves exponentially with cladding thickness.

X. MECHANISM OF 2D-3D HETEROSTRUCTURES

We have shown through the illustrations that 2D-3D heterostructures enable total confinement of light in planar microcircuits over a large frequency bandwidth, by careful selection of structural parameters. In this section, we present an interpretation of the underlying physics of the 2D-3D heterostructures. In particular, we provide an answer to the fundamental question: “What is the underlying mechanism for diffractionless high bandwidth light flow in the 2D microchip layer of the 2D-3D heterostructure?”

We begin by considering the conditions for high bandwidth microcircuitry. These are (1) the waveguide mode spans a large bandwidth (or the dispersion is not flat) and (2) the on-chip band gap is large. It is clear from Sec. IV that in

order to obtain a large bandwidth waveguide mode, the 2D PC layer has to be adequately thick. For the 2D-3D heterostructure with certain 2D PC layer thickness, we can obtain a maximal on-chip band gap by minimizing the bandwidth of the spurious planar defect modes (2D PC slab modes). This can be achieved when the fields of the planar defect modes are delocalized from (less confined in) the 2D PC slab region, since less confinement implies that the frequencies are near to the band edge (not deep inside the band gap). This, in turn, can be achieved when the field distributions in the 2D PC slab region and the 3D PBG region are well matched at the interfaces. Therefore, the 2D PC layer should be embedded into the 3D PBG materials at the cross section at which the field distribution is similar to that of the 2D PC. This turns out to be the position where the cross section itself resembles the 2D PC as will be shown in the followings, and thus our principle for the embedding position used in Secs. VI and VII.

To summarize the above statements, planar optical microchip functionality, in 3D PBG materials, requires the identification of a cutting plane where there exists one set of 3D eigenmodes whose field distributions (at that cross section) closely resembles the field distribution of a “complete” set of eigenmodes of the 2D PC spanning every in-plane wave vector. Mismatch of 2D and 3D field distributions leads to a filling in of the on-chip 3D PBG with spurious defect modes, whereas matching of the 2D and 3D field patterns facilitates confinement of the planar defect mode into the narrowest possible spectral range. When the 2D PC slab is inserted in between two semi-infinite 3D PBG materials at the prescribed cutting plane, the field distributions in both regions match well with each other, causing minimal local disruption of the 3D PBG. The resulting set of heterostructure modes, in turn, react to engineered point and line defects in the 2D PC slab region by forming three-dimensionally confined electromagnetic modes in a planar microcircuit within the on-chip 3D PBG.

We provide plausibility to the above conjecture by direct computation of electric field distributions in the 3D PBG cladding material and the 2D PC microchip layer comprising the inverse-opal-based heterostructure. In particular, we show the field distribution for the dielectric bands (bands below the band gap), responsible for microcavity and linear waveguide defect modes created by removing dielectric materials from the heterostructure. First, we show in Figs. 36(a) and 36(b), the band structures for the close-packed inverse opal structure and the infinitely high dielectric rods ($r = 0.22a$) in a triangular lattice 2D PC, respectively. For simplicity, the band diagrams are shown only for one crystalline direction (=direction of the waveguide). Since it is more convenient to describe the translational symmetry of the waveguide in a rectangular lattice (than in a triangular lattice), we use a rectangular lattice containing two dielectric rods in one unit cell for Fig. 36(b) and an orthorhombic lattice containing six air spheres in one unit cell for Fig. 36(a). There are six bands below the *second* 2D TM band gap [Fig. 36(b)], and forty-eight bands below the 3D PBG in the inverse opal structure [Fig. 36(a)]. Six bands of the inverse opal structure that correspond to the six bands of the triangular lattice 2D PC are indicated by solid lines. It is interesting to note that

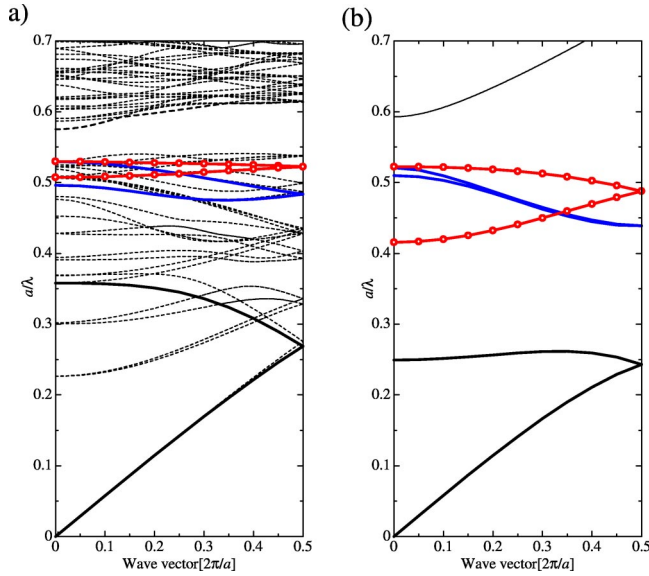


FIG. 36. Band diagrams for (a) the inverse opal 3D PBG material and (b) the triangular lattice of circular dielectric rods 2D PC. The band diagrams are shown only for one crystalline direction (=direction of the waveguide). There are six bands below the second order 2D TM band gap (b), and forty-eight bands below the 3D PBG in the inverse opal structure (a). Six bands of the inverse opal structure that correspond to the six bands of the triangular lattice 2D PC are indicated by thick solid lines (with circles).

the frequency range of the 3D PBG of the inverse opal structure is in the same range as the frequency range of the *second* 2D TM band gap of the triangular lattice 2D PC.

We show in Fig. 37 field patterns for the six dielectric bands of the 2D PC and the six corresponding bands of the inverse opal structure for the wave vector $k = (0.25, 0) 2\pi/a$. Clearly, the field patterns of the 3D PBG correspond well with those of the 2D PC. The two bands indicated by thick solid (red) lines with circles in Figs. 36(a) and 36(b) are responsible for the formation of the waveguide mode when a row of dielectric rods is removed. However, only the higher frequency band of these two bands enters the on-chip PBG as seen in Fig. 29.

We have presented above an explanation of defect-mode formation in 2D-3D heterostructures. A further question concerns the detailed requirements for formation of single-mode, air waveguides in 3D PBG materials. In particular, “Can optimally functional 2D PC-like, single-mode, air waveguides be created in the 3D PBG materials without recourse to a 2D-3D heterostructure?” For example, at the plane where two layers touch in the woodpile structure, the field resembles that of the 2D PC. It is tempting to argue that single-mode, air waveguides with 90° sharp bends in a single layer can be obtained directly from the 3D woodpile structure by removing dielectric materials from this plane and the positions nearby. However, our calculations show that such air defects do not yield an ideal, single-mode waveguide that spans the entire band gap. In fact, many modes are created inside the 3D PBG that do not have 2D-PC characteristics. The underlying reason is that although the field patterns at the chosen plane resemble those of the 2D PC, the field

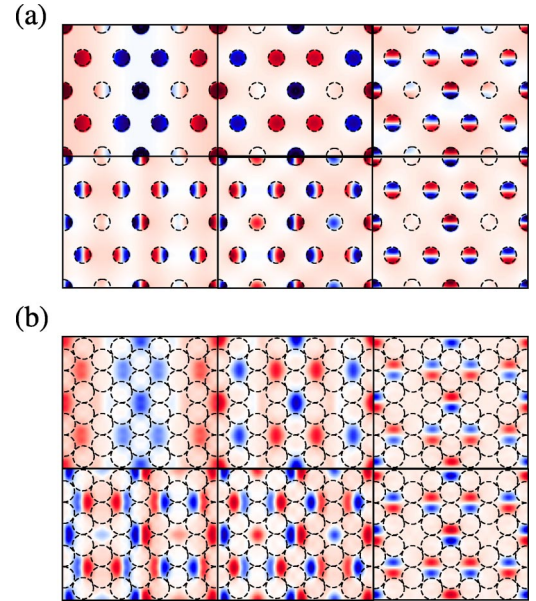


FIG. 37. Distributions for the z -component of electric displacement field of (a) the six dielectric bands in the 2D PC and (b) the corresponding six dielectric bands in the inverse opal 3D PBG at the optimized embedding position. The field patterns are shown for the wave vector $k = (0.25, 0) 2\pi/a$. The broken lines show geometry of the corresponding photonic crystal structures. Note that in (a), the areas inside circles correspond to dielectric but in (b), these correspond to air.

patterns at nearby planes do not resemble those of the 2D PC and thus contribute to creation of other spurious defect modes. In the 2D-3D heterostructure, the “2D-like” field distributions are “enhanced” by the insertion the 2D PC slab at the optimum position. This makes possible single-mode, air waveguides with almost completely lossless 90° sharp bends and many other microcircuit elements characteristic of an idealized (infinite aspect ratio) 2D photonic crystal [28].

XI. CONCLUSION

We have presented extensive analyses of a variety of 2D-3D heterostructures. On-chip, single-mode, waveguiding in air is demonstrated in the heterostructures based on the square spiral, woodpile, slanted pore, Yablonovite, and inverse opal 3D PBG materials. In particular, the heterostructures based on the square spiral, woodpile, and inverse opal 3D PBG materials are optimized to yield maximal single-mode waveguiding bandwidths. The waveguiding bandwidths of ~ 73 nm and 150–180 nm have been achieved for the inverse opal based heterostructure and for other types of heterostructures, respectively. We also demonstrated lossless propagation of light inside the optical microcircuit layer inside the heterostructure by 3D FDTD simulations. We examined the effects of fabrication-related disorder and showed that the heterostructure is robust to on-chip structural disorder and misalignment between the 2D and 3D photonic crystal layers. Finally, we provided a physical interpretation of the mechanism of the 2D-3D PBG heterostructure based optical microcircuitry. Certain modes in the 3D PBG materials

with electromagnetic field distribution, at specific cutting planes, resembling a “complete set” of 2D PC modes were found responsible for the diffractionless, on-chip, optical microcircuitry in the 2D-3D heterostructure. This suggests that many of the optical microcircuit elements presented earlier [28] in the context of idealized 2D photonic crystals can be readily incorporated into real 3D PBG materials, without the problem of leakage of light into the third dimension. Moreover, the 2D-3D PBG heterostructure enables “engineering

of the electromagnetic vacuum” for highly frequency selective control of spontaneous emission from atoms and the incorporation of novel active devices within the optical microchip.

ACKNOWLEDGMENT

This work was supported in part by the Natural Sciences and Engineering Research Council of Canada.

-
- [1] S. John, Phys. Rev. Lett. **58**, 2486 (1987).
 [2] E. Yablonovitch, Phys. Rev. Lett. **58**, 2059 (1987).
 [3] J. D. Joannopoulos, P. R. Villeneuve, and S. Fan, Nature (London) **386**, 143 (1997).
 [4] A. Mekis, J. C. Chen, I. Kurland, S. Fan, P. R. Villeneuve, and J. D. Joannopoulos, Phys. Rev. Lett. **77**, 3787 (1998).
 [5] S. Fan, P. R. Villeneuve, J. D. Joannopoulos, and H. A. Haus, Phys. Rev. Lett. **80**, 960 (1998).
 [6] A. Chutinan and S. Noda, Appl. Phys. Lett. **75**, 3739 (1999).
 [7] M. M. Sigalas, R. Biswas, K. M. Ho, C. M. Soukoulis, D. Turner, B. Vasiliu, S. C. Kothari, and S. Lin, Microwave Opt. Technol. Lett. **23**, 56 (1999).
 [8] A. R. Weily, L. Horvath, K. P. Esselle, and B. C. Sanders, Microwave Opt. Technol. Lett. **40**, 1 (2004).
 [9] A. Chutinan and S. Noda, Phys. Rev. B **62**, 4488 (2000).
 [10] S. Noda, K. Tomoda, N. Yamamoto, and A. Chutinan, Science **289**, 604 (2000).
 [11] M. L. Povinelli, S. G. Johnson, S. Fan, and J. D. Joannopoulos, Phys. Rev. B **64**, 075313 (2001).
 [12] G. Parker and M. Charlton, Phys. World **13** (August), 29 (2000).
 [13] S. John, Phys. Rev. Lett. **53**, 2169 (1984).
 [14] S. John and M. Florescu, J. Opt. A, Pure Appl. Opt. **3**, S103 (2001).
 [15] A. Chutinan, S. John, and O. Toader, Phys. Rev. Lett. **90**, 123901 (2001).
 [16] O. Toader and S. John, Science **292**, 1133 (2001).
 [17] O. Toader and S. John, Phys. Rev. E **66**, 016610 (2002).
 [18] S. R. Kennedy, M. J. Brett, H. Miguez, O. Toader, and S. John, Photonics and Nanostructures Fundamental and Applications **1**, 37 (2003).
 [19] K. M. Ho, C. T. Chan, C. M. Soukoulis, R. Biswas, and M. Sigalas, Solid State Commun. **89**, 413 (1994).
 [20] S. Y. Lin, J. G. Fleming, D. L. Hetherington, B. K. Smith, R. Biswas, K. M. Ho, and M. M. Sigalas, Nature (London) **394**, 251 (1998).
 [21] O. Toader, M. Berciu, and S. John, Phys. Rev. Lett. **90**, 233901 (2003).
 [22] E. Yablonovitch, T. J. Gmitter, and K. M. Leung, Phys. Rev. Lett. **67**, 2295 (1991).
 [23] K. Busch and S. John, Phys. Rev. E **58**, 3896 (1998).
 [24] A. F. Koenderink, Ph.D. thesis, University of Amsterdam, 2003.
 [25] A. Blanco *et al.*, Nature (London) **405**, 437 (2000).
 [26] J. N. Winn, Y. Fink, S. Fan, and J. D. Joannopoulos, Opt. Lett. **23**, 1573 (1998).
 [27] Y. Fink, J. N. Winn, S. Fan, C. Chen, J. Michel, J. D. Joannopoulos, and E. L. Thomas, Science **282**, 1679 (1998).
 [28] J. D. Joannopoulos, R. D. Meade, and J. N. Winn, *Photonic Crystals: Molding the Flow of Light* (Princeton University Press, Princeton, NJ, 1995).
 [29] *Handbook of Optical Constants of Solids*, edited by E. D. Palik (Academic, New York, 1985).
 [30] *Photonic Band Gaps and Localization*, edited by C. M. Soukoulis, Proceedings of the NATO Advanced Science Institutes Series (Plenum, New York, 1993).
 [31] K. S. Yee, IEEE Trans. Antennas Propag. **14**, 302 (1966).
 [32] G. Mur, IEEE Trans. Electromagn. Compat. **EMC-23**, 377 (1981).
 [33] K. Robbie and M. J. Brett, Nature (London) **384**, 616 (1996).
 [34] R. Z. Wang and S. John, Phys. Rev. A **70**, 043805 (2004).
 [35] A. Chutinan and S. Noda, Jpn. J. Appl. Phys., Part 1 **39**, 2353 (2000).
 [36] This problem is known to happen when one cannot collect the entire transmitted or reflected pulses before the reflection of itself comes back to spoil the data. It can be avoided by either using longer waveguides to delay such reflection or employ a better absorbing boundary condition to eliminate the reflection, both of which are technically challenging. From our experience, if we were able to eliminate this technical error, the “correct” value tends to converge to the average between the oscillation maxima and minima.
 [37] S. Noda, N. Yamamoto, and A. Sasaki, Jpn. J. Appl. Phys., Part 2 **35**, L909 (1996).
 [38] W. Bogaerts, P. Bienstman, and R. Baets, Opt. Lett. **28**, 689 (2003).
 [39] Y. Tanaka, T. Asano, Y. Akahane, B. S. Song, and S. Noda, Appl. Phys. Lett. **82**, 1661 (2003).
 [40] J. S. I, Y. Park and H. Jeon, J. Korean Phys. Soc. **39**, 994 (2001).
 [41] T. Ochiai and K. Sakoda, Phys. Rev. B **63**, 125107 (2001).